Eur. Phys. J. A (2018) **54**: 210
DOI 10.1140/epja/i2018-12643-x

THE EUROPEAN PHYSICAL JOURNAL A

Regular Article – Theoretical Physics

Eta and etaprime photoproduction on the nucleon with the isobar model EtaMAID2018

L. Tiator[1,a], M. Gorchtein[1], V.L. Kashevarov[1], K. Nikonov[1], M. Ostrick[1], M. Hadžimehmedović[2], R. Omerović[2], H. Osmanović[2], J. Stahov[2], and A. Švarc[3]

[1] Institut für Kernphysik, Johannes Gutenberg-Universität Mainz, D-55099 Mainz, Germany
[2] University of Tuzla, Faculty of Natural Sciences and Mathematics, Univerzitetska 4, 75000 Tuzla, Bosnia and Herzegovina
[3] Rudjer Bošković Institute, Bijenička cesta 54, P.O. Box 180, 10002 Zagreb, Croatia

Received: 13 July 2018 / Revised: 2 October 2018
Published online: 6 December 2018
© Società Italiana di Fisica / Springer-Verlag GmbH Germany, part of Springer Nature, 2018
Communicated by U.-G. Meißner

Abstract. The isobar model EtaMAID has been updated with new and high precision data for η and η' photoproduction on protons and neutrons from MAMI, ELSA, GRAAL and CLAS. The background is described in a recently developed Regge cut model, and for the resonance part the whole list of nucleon resonances has been investigated with 21 N^* states contributing to η photoproduction and 12 N^* states contributing to η' photoproduction. A new approach is discussed to avoid double counting in the overlap region of Regge and resonances. A comparison is done among four newly updated partial waves analyses for observables and partial waves. Finally, the possibility of a narrow resonance near $W = 1900\,\text{MeV}$ is discussed, that would be able to explain unexpected energy and angular dependence of observables in $p(\gamma,\eta')p$ near η' threshold.

1 Introduction

The photo-induced production of η and η' mesons is a selective probe to study excitations of the nucleon. These mesons represent the isoscalar members of the fundamental pseudoscalar-meson nonet and, in contrast to the isovector π, excitations with isospin $I = 3/2$ (Δ resonances) do not decay into ηN and $\eta' N$ final states. An overview of the current status of nucleon resonances can be found in ref. [1] and of the experimental and phenomenological progress in η photoproduction can be found in ref. [2].

The isobar model EtaMAID is part of the Mainz MAID project [3–5] with online programs performing real-time calculations of observables, amplitudes and partial waves (multipoles). EtaMAID was introduced in 2001 [6] as a model with eight prominent nucleon resonances: $N(1535)\frac{1}{2}^-(S_{11})$, $N(1650)\frac{1}{2}^-(S_{11})$, $N(1710)\frac{1}{2}^+(P_{11})$, $N(1720)\frac{3}{2}^+(P_{13})$, $N(1520)\frac{3}{2}^-(D_{13})$, $N(1700)\frac{3}{2}^-(D_{13})$, $N(1675)\frac{5}{2}^-(D_{15})$, and $N(1680)\frac{5}{2}^+(F_{15})$ (see footnote[1]). The background was modeled with Born terms and t-channel vector meson exchanges of ω and ρ mesons. The model was developed for photo- and electroproduction on protons and neutrons and was well fitted to the few available data in 2001. Since that time a lot of developments occurred, first of all for the experimental data base.

There was a huge effort at several accelerator facilities to combine high intensity polarized photon beams with modern 4π detectors and spin-polarized targets. In particular, the Crystal Ball/TAPS setup at MAMI in Mainz (Germany) [7], the Crystal Barrel/TAPS at ELSA in Bonn (Germany) [8], and the CLAS detector at JLab in Newport News (USA) [9] have reached this goal and provided new, valuable information about photo-induced η and η' production. At the GRAAL facility in Grenoble (France) [10] and the LEPS facility at SPring-8 in Osaka (Japan) [11], photon beams with high linear polarization are available via laser-backscattering and also data from ELPH at Tohoku University in Sendai (Japan) [12] became available. The CLAS detector was using a magnetic field in order to reconstruct the recoiling proton with high resolution. The final state neutral mesons were identified via a missing mass analysis. The other detectors used electromagnetic calorimeters with almost 4π coverage to detect photons, pions, protons and neutrons. The $\gamma N \to \eta N$ and $\gamma N \to \eta' N$ reactions were identified via a combination of missing mass and invariant mass techniques.

[a] e-mail: tiator@uni-mainz.de

[1] Throughout this paper we will use two notations for nucleon resonances, the general notation $N(1535)\frac{1}{2}^-$, introduced by PDG in 2012, and the older πN notation as $S_{11}(1535)$.

Photoproduction of η or η' on the nucleon has been studied in various theoretical approaches, in quark models [13–15], Lagrangian models [16, 17], effective field theory [18, 19], dispersion theoretical calculations [20, 21], Regge models [22], isobar models [6, 20, 23–27], and combined analyses by using the additional information from NN interaction [28, 29]. Most flexible and successful have been isobar models, where nucleon resonances are treated in s-channel Breit-Wigner parametrization with energy-dependent widths due to the coupling with other decay channels. The non-resonant background in those models is described by s- and u-channel Born terms and t-channel vector meson exchanges.

Besides single-channel investigations, a series of coupled-channel partial wave analyses (PWA) [7, 30–34] have been performed with multiple channels as πN, σN, $\pi\Delta$, ηN, $K\Lambda$, $K\Sigma$, ρN, ωN, and $\eta' N$. Within the last few months, new updates have been obtained by the Bonn-Gatchina group [35], the Jülich-Bonn group [36] and the Kent State University group [37].

All these PWA are energy-dependent (ED) analyses, where an underlying model determines the functional dependence on the energy and provides continuity and, in an optimal case, also analyticity of the partial wave amplitudes. An energy-independent or single-energy (SE) PWA is free of such a model dependence but depends very much on the availability of a "complete experiment" [38] and on analyticity and unitarity constraints. This has been done very successfully for πN scattering and pion photoproduction. For ηN photoproduction such constraints are mostly unavailable, making a single-energy PWA much more difficult and can lead to ambiguous solutions. In a very recent work, we have accomplished such a SE PWA for η photoproduction using constraints from fixed-t analyticity [39].

The last update of EtaMAID was done in 2003 [6] with a Reggeized isobar model for $p(\gamma,\eta)p$ and an extension to $p(\gamma,\eta')p$ was established for the threshold region, when new data on differential cross sections became available from SAPHIR at ELSA in Bonn [40].

Combining Reggeized t-channel exchanges with resonances in the direct channel is by no means a new idea, see *e.g.* the model of ref. [41] for charge-exchange πN scattering or models for meson photoproduction, *e.g.* EtaMAID2003 [6] or Regge-plus-resonance approach for $K\Lambda$ photoproduction [42]. In these models, the Regge amplitude is obtained from a fit to high energy data and continued into the resonance region. For η and especially η' production the Regge regime that sets in at $W \geq 2.5\,\mathrm{GeV}$ is quite close to the accessible part of the resonance region. Matching the invariant amplitudes that are obtained from the low-energy fit onto Regge amplitude thus represents a valuable physics constraint. The advantage from the technical point of view is that it is not necessary to introduce many free parameters which would have been necessary to fix the non-resonant background amplitude, so only resonance parameters are used as fit parameters.

However, it has been realized early on that when projected on the s-channel partial waves, Regge amplitudes generate resonance-like Schmid loops on the Argand diagram for each partial wave [43], which leads to a general problem of double counting in the extraction of resonance parameters. Collins *et al.* [44] pointed out that to state a correspondence between Regge asymptotic and s-channel resonances, one would have to invoke unitarity, as per finite energy sum rules (FESR), see *e.g.* ref. [45] for an early application to πN scattering.

With these reservations in mind, we pursue here another method which uses as background the Regge amplitude with kinematical suppression factor applied in the resonance region. This damping factor is needed to at least partially remove the double counting. To address this double counting in detail the FESR is the most natural tool, and we postpone this study to the upcoming work. Moreover, in view of the ambiguity Regge-resonances we opt not to discuss the Breit-Wigner resonance parameters returned by the fit in detail.

Independent whatever procedure is applied, the resonance parametrization using Breit-Wigner amplitudes remains model dependent. Generalized Breit-Wigner amplitudes have enough freedom with the energy dependence of the widths and of the vertex functions, that changes in the background can usually be absorbed by the resonance contributions, therefore leading to sizeable model uncertainties to masses, widths, branching ratios and photo couplings. In careful treatments, and for resonances with widths $\Gamma \lesssim 120\,\mathrm{MeV}$, the model dependence is rather mild. Therefore, PDG [1] decided to keep such traditional resonance parameters, even if the spread of values is often quite large. First priority in newer PWA are the fundamental t-matrix pole positions and residues of various elastic and inelastic reactions involving nucleon resonance excitations. In an upcoming work we will use our obtained partial waves and analyze nucleon resonances by its pole position and residues with the Laurent-plus-Pietarinen (L+P) method [46, 47].

The paper is organized as follows. In sect. 2 we will first give the basic formalism for kinematics, amplitudes and observables. In sect. 3 we present the details of our isobar model. We shortly describe the Regge cut model which has already been published and give our formulation for nucleon resonance excitations. In sect. 4 we present our results on η and η' photoproduction from protons and neutrons with comparisons to the data and PWA from other analysis groups. In sect. 5 we discuss a recent attempt to search for a narrow N^* resonance near the η' threshold. Partial waves are compared with recent solutions by the Bonn-Gatchina, Jülich-Bonn and Kent State University groups in sect. 6, before we summarize our method and results in sect. 7. In an appendix we give the formulas for polarization observables used in our analysis and tables of our background and Breit-Wigner resonance parameters.

2 Formalism

2.1 Kinematics in η photoproduction

For η photoproduction on the nucleon, we consider the reaction

$$\gamma(k) + N(p_i) \to \eta(q) + N'(p_f), \tag{1}$$

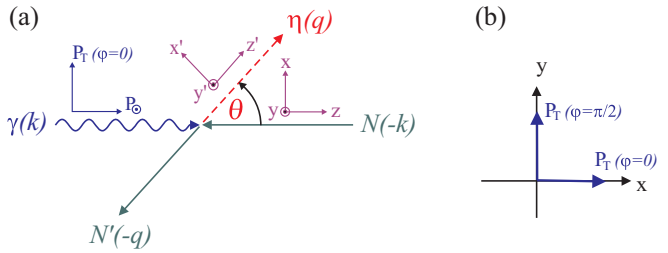

Fig. 1. Kinematics of photoproduction and frames for polarization. The frame $\{x, y, z\}$ is used for target polarization $\{P_x, P_y, P_z\}$, whereas the recoil polarization $\{P_{x'}, P_{y'}, P_{z'}\}$ is defined in the frame $\{x', y', z'\}$, which is rotated around $y' = y$ by the polar angle θ. The azimuthal angle φ is defined in the $\{x, y\}$ plane (b) and is zero in the projection shown in the figure (a).

where the variables in brackets denote the four-momenta of the participating particles. These are $k^\mu = (k, \mathbf{k})$, $q^\mu = (\omega, \mathbf{q})$ for photon and η meson, and $p_i^\mu = (E_i, \mathbf{p}_i)$, $p_f^\mu = (E_f, \mathbf{p}_f)$ for incoming and outgoing nucleon, respectively. The familiar Mandelstam variables are given as

$$s = W^2 = (p_i + k)^2, \qquad t = (q - k)^2, \qquad u = (p_i - q)^2, \tag{2}$$

the sum of the Mandelstam variables is given by the sum of the external masses

$$s + t + u = 2m_N^2 + m_\eta^2, \tag{3}$$

where m_N and m_η are masses of proton and η meson, respectively. The crossing symmetrical variable is

$$\nu = \frac{s - u}{4m_N}. \tag{4}$$

In the ηN center-of-mass (c.m.) system, we have $\mathbf{p}_i = -\mathbf{k}$, $\mathbf{p}_f = -\mathbf{q}$, and the energies and momenta can be related to the Mandelstam variable s by

$$k = |\mathbf{k}| = \frac{s - m_N^2}{2\sqrt{s}}, \qquad \omega = \frac{s + m_\eta^2 - m_N^2}{2\sqrt{s}}, \tag{5}$$

$$q = |\mathbf{q}| = \left[\left(\frac{s - m_\eta^2 + m_N^2}{2\sqrt{s}}\right)^2 - m_N^2\right]^{\frac{1}{2}}, \tag{6}$$

$$E_i = \frac{s + m_N^2}{2\sqrt{s}}, \qquad E_f = \frac{s + m_N^2 - m_\eta^2}{2\sqrt{s}}, \tag{7}$$

$W = \sqrt{s}$ is the c.m. energy. Furthermore, we will also refer to the lab energy of the photon, $E = (s - m_N^2)/(2m_N)$.

2.2 Cross section and polarization observables

As depicted in fig. 1, the photon polarization can be linear or circular. For a linear photon polarization ($P_T = 1$) along the direction $\hat{\mathbf{x}}$ we define the azimuthal angle $\varphi = 0$, and perpendicular, in direction $\hat{\mathbf{y}}$, the polarization angle is $\varphi = \pi/2$. For right-handed circular polarization $P_\odot = +1$.

We may classify the differential cross sections by the three classes of double polarization experiments and one class of triple polarization experiments, which, however, do not give additional information:

– polarized photons and polarized target

$$\begin{aligned}\frac{\mathrm{d}\sigma}{\mathrm{d}\Omega} = \sigma_0 \{&1 - P_T \Sigma \cos 2\varphi \\ &+ P_x (-P_T H \sin 2\varphi + P_\odot F) \\ &+ P_y (T - P_T P \cos 2\varphi) \\ &+ P_z (P_T G \sin 2\varphi - P_\odot E)\},\end{aligned} \tag{8}$$

– polarized photons and recoil polarization

$$\begin{aligned}\frac{\mathrm{d}\sigma}{\mathrm{d}\Omega} = \sigma_0 \{&1 - P_T \Sigma \cos 2\varphi \\ &+ P_{x'} (-P_T O_{x'} \sin 2\varphi - P_\odot C_{x'}) \\ &+ P_{y'} (P - P_T T \cos 2\varphi) \\ &+ P_{z'} (-P_T O_{z'} \sin 2\varphi - P_\odot C_{z'})\},\end{aligned} \tag{9}$$

– polarized target and recoil polarization

$$\begin{aligned}\frac{\mathrm{d}\sigma}{\mathrm{d}\Omega} = \sigma_0 \{&1 + P_y T + P_{y'} P + P_{x'} (P_x T_{x'} - P_z L_{x'}) \\ &+ P_{y'} P_y \Sigma + P_{z'} (P_x T_{z'} + P_z L_{z'})\}.\end{aligned} \tag{10}$$

In these equations σ_0 denotes the unpolarized differential cross section. Instead of asymmetries, in the following we will also discuss the product of the unpolarized cross section with the asymmetries and will use the notation $\check{\Sigma} = \sigma_0 \Sigma$, $\check{T} = \sigma_0 T, \cdots$. In appendix A we give expressions of the observables in terms of CGLN amplitudes.

2.3 Invariant amplitudes

The nucleon electromagnetic current for pseudoscalar meson photoproduction can be expressed in terms of four invariant amplitudes A_i [48],

$$J^\mu = \sum_{i=1}^{4} A_i(\nu, t)\, M_i^\mu, \tag{11}$$

with the gauge-invariant four-vectors M_i^μ given by

$$\begin{aligned}M_1^\mu &= -\frac{1}{2} i\gamma_5 (\gamma^\mu \not{k} - \not{k}\gamma^\mu), \\ M_2^\mu &= 2i\gamma_5 \left(P^\mu\, k \cdot \left(q - \frac{1}{2}k\right) - \left(q - \frac{1}{2}k\right)^\mu k \cdot P\right), \\ M_3^\mu &= -i\gamma_5 (\gamma^\mu\, k \cdot q - \not{k} q^\mu), \\ M_4^\mu &= -2i\gamma_5 (\gamma^\mu\, k \cdot P - \not{k} P^\mu) - 2m_N\, M_1^\mu,\end{aligned} \tag{12}$$

where $P^\mu = (p_i^\mu + p_f^\mu)/2$, and the gamma matrices are defined as in ref. [49].

The nucleon pole terms for $N(\gamma,\eta)N$, $A_i^{I,pole}$ $(I = +,0)$ are given by

$$\begin{aligned}
A_1^{I,pole} &= \frac{e\,g_{\eta N}}{2}\left(\frac{1}{s-m_N^2}+\frac{1}{u-m_N^2}\right),\\
A_2^{I,pole} &= -\frac{e\,g_{\eta N}}{t-m_\eta^2}\left(\frac{1}{s-m_N^2}+\frac{1}{u-m_N^2}\right),\\
A_3^{I,pole} &= -\frac{e\,g_{\eta N}}{2m_N}\frac{\kappa^{(I)}}{2}\left(\frac{1}{s-m_N^2}-\frac{1}{u-m_N^2}\right),\\
A_4^{I,pole} &= -\frac{e\,g_{\eta N}}{2m_N}\frac{\kappa^{(I)}}{2}\left(\frac{1}{s-m_N^2}+\frac{1}{u-m_N^2}\right), \qquad (13)
\end{aligned}$$

with $\kappa^{(+)} = \kappa_p - \kappa_n$, and $\kappa^{(0)} = \kappa_p + \kappa_n$, where κ_p and κ_n are the anomalous magnetic moments of the proton and the neutron, respectively.

2.4 CGLN amplitudes and multipoles

For PWA the CGLN amplitudes $F_i(W,x)$ [48] are conveniently used. They are defined in the c.m. frame using Coulomb gauge. The matrix element $\mathcal{F}$ with the $e.m.$ current of eq. (11) then reads

$$\begin{aligned}
\mathcal{F} &= -\epsilon_\mu J^\mu\\
&= i\,(\vec{\sigma}\cdot\hat{\epsilon})\,F_1 + (\vec{\sigma}\cdot\hat{q})\,(\vec{\sigma}\times\hat{k})\cdot\hat{\epsilon}\,F_2 + i\,(\hat{\epsilon}\cdot\hat{q})\,(\vec{\sigma}\cdot\hat{k})F_3\\
&\quad + i(\hat{\epsilon}\cdot\hat{q})(\vec{\sigma}\cdot\hat{q})\,F_4, \qquad (14)
\end{aligned}$$

where $\epsilon^\mu = (0,\vec{\epsilon})$ and $\vec{\epsilon}\cdot\vec{k} = 0$. In partial wave analysis of pseudoscalar meson photoproduction it is convenient to work with CGLN amplitudes giving simple representations in terms of electric and magnetic multipoles and derivatives of Legendre polynomials

$$\begin{aligned}
F_1(W,x) &= \sum_{l=0}^{\infty}[(lM_{l+}(W)+E_{l+}(W))P'_{l+1}(x)\\
&\quad +((l+1)M_{l-}(W)+E_{l-}(W))P'_{l-1}(x)],\\
F_2(W,x) &= \sum_{l=1}^{\infty}[(l+1)M_{l+}(W)+lM_{l-}(W)]P'_l(x),\\
F_3(W,x) &= \sum_{l=1}^{\infty}[(E_{l+}(W)-M_{l+}(W))P''_{l+1}\\
&\quad +(E_{l-}(W)+M_{l-}(W))P''_{l-1}(x)],\\
F_4(W,x) &= \sum_{l=2}^{\infty}[M_{l+}(W)-E_{l+}(W)-M_{l-}(W)\\
&\quad -E_{l-}(W)]P''_l(x), \qquad (15)
\end{aligned}$$

where $x = \cos\theta$ is the cosine of the scattering angle. In appendix B we give relations between the CGLN and the invariant amplitudes.

3 The isobar model

In the isobar model the photoproduction amplitudes of η and η' mesons are written in terms of nucleon resonance excitations in generalized Breit-Wigner forms and in non-resonant background amplitudes. For simplicity we write all formulas in terms of (γ,η). For (γ,η') all those formulas and kinematical relations can easily be extended.

For a specific partial wave $\alpha = \alpha(\ell, j = \ell \pm 1/2, \mathcal{M})$, where ℓ is the angular momentum of the ηN system in the final state, j is the total spin and $\mathcal{M}$ stands either for an electric (E) or magnetic (M) transition. The total partial wave amplitude can be written as a sum of a background amplitude $t^{\alpha,b}$ and a resonance amplitude $t^{\alpha,r}$

$$t^{\alpha}_{\gamma,\eta}(W) = t^{\alpha,b}_{\gamma,\eta}(W) + t^{\alpha,r}_{\gamma,\eta}(W). \qquad (16)$$

In photoproduction we identify the partial wave amplitudes directly with the electromagnetic multipoles $E_{\ell\pm}$ and $M_{\ell\pm}$.

3.1 The non-resonant background

Traditionally, the background amplitude is taken as a sum of Born terms and t-channel meson exchange contributions

$$t^{\alpha,b}_{\gamma,\eta}(W) = t^{\alpha,Born}_{\gamma,\eta}(W) + t^{\alpha,VM}_{\gamma,\eta}(W). \qquad (17)$$

The Born terms for η and η' photoproduction play a minor role due to the small coupling constants. Whereas the πNN coupling is very large, $g^2_{\pi NN}/4\pi \approx 14$, for η and η' photoproduction $g^2_{\eta NN}/4\pi \sim g^2_{\eta' NN}/4\pi \lesssim 0.1$. This is a rather old observation [50] in contradiction to $SU(3)$ symmetry, where the coupling constants are predicted in the range of 1.

In all η photoproduction analyses this suppression of the Born terms has been confirmed and extensive studies have even found $g^2_{\eta NN}/4\pi \leq 10^{-3}$ [29]. For the $\eta' NN$ coupling our value is in agreement with a combined analysis including also $NN\eta'$ [28]. Nevertheless, in interference terms and at high energies, the Born terms can play some role, and similarly to our previous EtaMAID models, the couplings are determined in the fits to the data. The Born terms are most easily expressed in terms of invariant amplitudes and in pseudoscalar coupling they are given by the nucleon pole terms, eq. (13).

As our goal in the 2018 update is a continuous description of photoproduction from threshold up to the highest energies, where experimental data exists ($W \sim 5$ GeV), we introduced an energy dependence (damping) in order to suppress the strong rise of the Born terms, and therefore a violation of unitarity at high energies by

$$g_{\eta N} \to g_{\eta N}\left(\frac{W_{thr}}{W}\right)^{\alpha_B}, \qquad (18)$$

where α_B will be found in the fit to the data. Ideally, a correct high-energy behavior for the Born contribution should be achieved by replacing the single nucleon exchange in the u-channel by a Regge exchange of the nucleon trajectory. Such a modification alone would, however, violate gauge invariance and a more elaborate approach needs to be applied. We leave this to an upcoming work.

For t-channel exchanges the invariant amplitudes for vector and axial-vector poles are given by

$$A_1(t) = \frac{e\,\lambda_V\,g_V^{\mathfrak{t}}}{2m_\eta M_N}\,\frac{t}{t-M_V^2}\,, \tag{19}$$

$$A_2'(t) = -\frac{e\,\lambda_A\,g_A^{\mathfrak{t}}}{2m_\eta M_N}\,\frac{t}{t-M_A^2}\,, \tag{20}$$

$$A_3(t) = \frac{e\,\lambda_A\,g_A^{v}}{m_\eta}\,\frac{1}{t-M_A^2}\,, \tag{21}$$

$$A_4(t) = \frac{-e\,\lambda_V\,g_V^{v}}{m_\eta}\,\frac{1}{t-M_V^2}\,, \tag{22}$$

where $\lambda_{V(A)}$ denotes the electromagnetic coupling of the vector (V) or axial (A) vector mesons with masses $M_{V(A)}$. The constants $g_{V(A)}^{v(\mathfrak{t})}$ denote their vector (v) or tensor ($\mathfrak{t}$) couplings to the nucleon. In order to separate the vector and tensor contributions from individual mesons we have used the amplitude

$$A_2'(t) = A_1(t) + t\,A_2(t), \tag{23}$$

which has only contributions from the tensor coupling of an axial vector exchange.

Unlike in pion production, the physical region for η and especially η' production starts at considerably high energy. It is generally expected that already at $\nu \sim 2\,\mathrm{GeV}$ the low-t data are well-represented by Regge exchanges. At the same time, a model with simple vector exchanges becomes inadequate at high energy: a spin-1 exchange leads to a linearly increasing amplitude which violates unitarity, so one is forced to introduce phenomenological form factors to suppress this behavior.

To make use of all the data available for η photoproduction we propose here an alternative approach: a background function that is smoothly joined onto a Regge amplitude at high energy, but is modified in the resonance region to accommodate the nucleon resonances by avoiding double counting.

For the Regge amplitudes we follow our recent work on Regge phenomenology in π^0 and η photoproduction, ref. [51]. In that work we compared and discussed four solutions, different in the Regge formulation and in the data sets used in the fits. Here for EtaMAID we use our preferred solution I, a Regge cut model, where the full data set was fitted.

Technically, the t-channel exchange of Regge trajectories is done by replacing the single meson propagator by the following expression

$$\frac{1}{t-M^2} \Rightarrow D(s,t) = \left(\frac{s}{s_0}\right)^{\alpha(t)-1} \frac{\pi\,\alpha'}{\sin[\pi\alpha(t)]}\,\frac{\mathcal{S}+e^{-i\pi\alpha(t)}}{2}\,\frac{1}{\Gamma(\alpha(t))}\,, \tag{24}$$

where M is the mass of the Reggeon, $\mathcal{S}$ is the signature of the Regge trajectory ($\mathcal{S}=-1$ for vector and axial-vector mesons), and s_0 is a mass scale factor, commonly set to $1\,\mathrm{GeV}^2$. The Gamma function $\Gamma(\alpha(t))$ is introduced to suppress additional poles of the propagator.

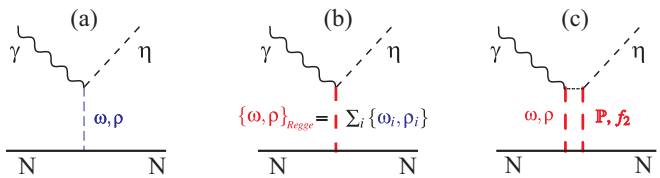

Fig. 2. t-channel contributions to η photoproduction from single poles (a), Regge poles (b), and Regge cuts (c). An example for ρ and ω meson exchange and $\mathbb{P}$ (Pomeron) and f_2 mesons for rescattering of two Reggeons.

In addition Regge cuts are added in our model. The Regge cuts can be understood as a rescattering effect at high energies, *e.g.* an η is produced via a vector or axial vector exchange at the first step, and then rescattered via a Pomeron or tensor exchange. This effect is shown in fig. 2(c) as contracted box diagrams, where two trajectories are exchanged consequently.

The trajectories for f_2 and $\mathbb{P}$ are shown in fig. 3(b) together with four cut trajectories $\rho\mathbb{P}$, $\omega\mathbb{P}$ (black solid and dashed lines) and ρf_2, ωf_2 (blue solid and dashed lines). Parameters of the Reggeon and cut trajectories used in the present work are given in our previous paper [51].

All four Regge cuts can contribute to vector and axial vector exchanges and can be written in the following form [52]:

$$D_{cut} = \left(\frac{s}{s_0}\right)^{\alpha_c(t)-1} e^{-i\pi\alpha_c(t)/2}\,e^{d_c t}. \tag{25}$$

In total, the vector meson propagators are replaced by

$$D_V \Rightarrow D_V + c_{V\mathbb{P}}\,D_{V\mathbb{P}} + c_{Vf_2}\,D_{Vf_2}, \quad V=\rho,\omega \tag{26}$$

and the axial vector meson propagators are replaced by

$$D_A \Rightarrow D_A + \sum_{V=\rho,\omega} (\tilde{c}_{V\mathbb{P}}\,D_{V\mathbb{P}} + \tilde{c}_{Vf_2}\,D_{Vf_2}), \quad A=b_1,h_1, \tag{27}$$

where the coefficients $c_{V\mathbb{P}}, c_{Vf_2}$ are for natural parity cuts and $\tilde{c}_{V\mathbb{P}}, \tilde{c}_{Vf_2}$ for unnatural parity cuts and are obtained by a fit to the data.

In detail, the invariant amplitudes will be changed in the following way

$$\begin{aligned}
&\lambda_\rho\,g_\rho^{v,\mathfrak{t}}\,\frac{1}{t-M_\rho^2} \to \lambda_\rho\,g_\rho^{v,\mathfrak{t}} \\
&\qquad [D_\rho(s,t) + c_{\rho\mathbb{P}}\,D_{\rho\mathbb{P}}(s,t) + c_{\rho f}\,D_{\rho f}(s,t)], \\
&\lambda_\omega\,g_\omega^{v,\mathfrak{t}}\,\frac{1}{t-M_\omega^2} \to \lambda_\omega\,g_\omega^{v,\mathfrak{t}} \\
&\qquad [D_\omega(s,t) + c_{\omega\mathbb{P}}\,D_{\omega\mathbb{P}}(s,t) + c_{\omega f}\,D_{\omega f}(s,t)], \\
&\lambda_{b_1}\,g_{b_1}^{\mathfrak{t}}\,\frac{1}{t-M_{b_1}^2} \to \lambda_{b_1}\,g_{b_1}^{\mathfrak{t}}\,D_{b_1}(s,t) \\
&\qquad +\lambda_\rho\,g_\rho^{\mathfrak{t}}\,[\tilde{c}_{\rho\mathbb{P}}\,D_{\rho\mathbb{P}}(s,t) + \tilde{c}_{\rho f_2}\,D_{\rho f_2}(s,t)] \\
&\qquad +\lambda_\omega\,g_\omega^{\mathfrak{t}}\,[\tilde{c}_{\omega\mathbb{P}}\,D_{\omega\mathbb{P}}(s,t) + \tilde{c}_{\omega f_2}\,D_{\omega f_2}(s,t)].
\end{aligned} \tag{28}$$

In practical calculations, it turns out that the axial vector Regge pole contributions, proportional to D_A, can

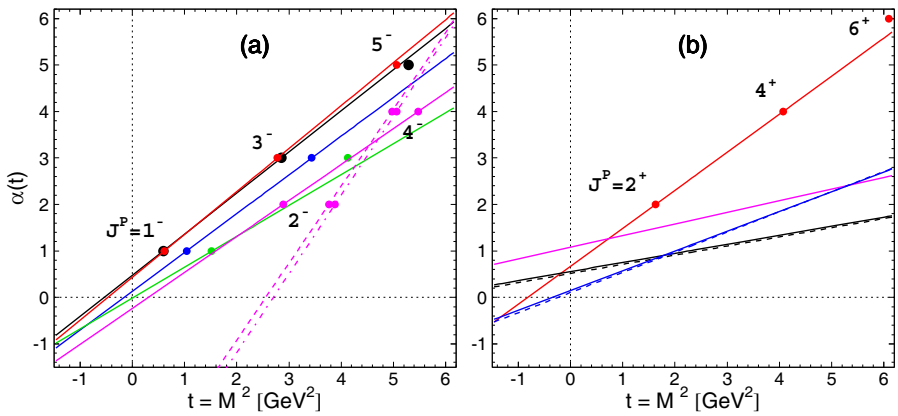

Fig. 3. Regge trajectories: (a) ρ black, ω red, ϕ blue, b_1 and h_1 green, ρ_2 and ω_2 magenta; dashed and dash-dotted magenta lines are ρ_2 and ω_2 of ref. [53,54]; (b) f_2 red, $\mathbb{P}$ magenta, ρf_2 black solid, ωf_2 blue dashed, $\rho\mathbb{P}$ black solid, $\omega\mathbb{P}$ black dashed.

be neglected, but the axial vector Regge cuts arising from ρ and ω together with $\mathbb{P}$ and f_2 are very important, in particular for polarization observables, as the photon beam asymmetry Σ.

The Regge cuts also allow us to describe a long standing problem of suitable candidates for an A_3 amplitude. While vector and axial-vector single pole or Regge pole exchanges do not contribute, Regge cut exchanges ρf_2 and ωf_2 satisfy all conservation law requirements. On the other hand, the $\rho\mathbb{P}$ and $\omega\mathbb{P}$ cuts do not contribute to the A_3 amplitude.

The main aspect in EtaMAID is the exploration of nucleon resonance excitation. Adding Regge amplitudes and resonances together, one runs into the well-known double-counting problem. The duality principle states that the full amplitude can be obtained by summing an infinite tower of either s- or t-channel resonances. In isobar models only a finite number of nucleon resonances are considered in the s-channel, still one cannot fully avoid this problem. Various methods have been discussed in the literature to treat with that problem. The so-called Regge-plus-Resonance models simply ignore double counting. In another approach, applied *e.g.* in EtaMAID2003 [6] and in the Bonn-Gatchina model [34], the lowest partial waves, where s-channel resonances are added, were projected out of the Regge amplitudes. In models where a lot of nucleon resonances are taken into account, this would, however, lead to an almost completely removed background amplitude in the resonance region. Recently, the concept of finite-energy sum rules was discussed and applied to π^0 and η photoproduction [55, 56], where resonance and Regge regions can be well separated and smoothly matched together. Those applications for η photoproduction are still in progress.

Here we want to apply a further method, where the double counting is removed by introducing a damping factor $F_d(W)$ to the Regge amplitudes, which goes to zero at η threshold and approaches unity above some energy,

$$A_i^{Regge} \to A_i^{Regge} \cdot F_d(W) \tag{29}$$

$$\text{with} \quad F_d(W) = \left(1 - e^{-\frac{W-W_{thr}}{\Lambda_R}}\right)\theta(W - W_{thr}). \tag{30}$$

The scale Λ_R describes at which energy Regge description fully sets in and is obtained in the fit. For a very small Λ_R the damping factor introduced above is a step function, whereas for large Λ_R it only approaches unperturbed Regge asymptotically. The way this damping factor cures the double counting problem can be seen as follows. Assume that an exact dual representation of the scattering amplitude t is realized and entails an infinite sum over the entire resonance spectrum in either s- or t-channel,

$$t = \sum_{i=1}^{\infty} t_s^{Res_i} = \sum_{i=1}^{\infty} t_t^{Res_i}. \tag{31}$$

At high s-channel energy, the t-channel sum can actually be performed in terms of an exchange of a few leading Regge trajectories α_i, $t^{Regge} \sim \sum_i c_i \nu^{\alpha_i}$. For the s-channel resonances, in turn, accounting for the full spectrum is not possible, and we limit ourselves to explicitly including only the lowest resonances up to $i = N$. We write

$$\begin{aligned} t &= \sum_{i=1}^{N} t_s^{Res_i} + \left[\sum_{i=1}^{\infty} t_t^{Res_i} - \sum_{i=1}^{N} t_s^{Res_i}\right] \\ &\approx \sum_{i=1}^{N} t_s^{Res_i} + F_d(W) t^{Regge}. \end{aligned} \tag{32}$$

The exact balance between the s-channel resonances and the part of the Regge amplitude removed by the damping factor can be controlled explicitly by the FESR. We will address these in an upcoming work. Parameters for the background can be found in table 7 in appendix C.

3.2 Nucleon resonance excitations

For a given partial wave α, a set of N_α nucleon resonances are added as generalized Breit-Wigner (BW) functions

Table 1. Threshold energies in MeV of various N^* decay channels.

πN	$\pi\pi N$	ηN	$K\Lambda$	$K\Sigma$	ωN	$\eta' N$
1077.84	1217.41	1486.13	1609.36	1686.32	1720.92	1896.05

with a unitary phase ϕ for each resonance,

$$t^{\alpha,r}_{\gamma,\eta}(W) = \sum_{j=1}^{N_\alpha} t^{\alpha,BW,j}_{\gamma,\eta}(W)\, e^{i\phi_j} \,. \tag{33}$$

Due to the weakness of photoproduction, where the moduli of the t-matrices are typically of the order 10^{-2} or smaller, a simple addition of multiple resonances is sufficient and does not violate unitarity. The phase ϕ_j introduced in eq. (33) is new for our EtaMAID models but was always applied in pion photo- and electroproduction. Whereas in (γ,π) the Watson theorem determines the phase ϕ_j at least below the $\pi\pi$ threshold, in η and η' production we have no theoretical guideline and use ϕ_j as a fit parameter. Furthermore, ϕ_j will be a constant in this work, while in general it can be an energy-dependent function with proper threshold behavior. The phase ϕ_j is often also called the "background phase", because it is indirectly determined by the background, which is different for the different channels ηp, ηn, $\eta' p$, $\eta' n$ and also different for electric and magnetic multipoles.

For a given partial wave α, the relevant multipoles $\mathcal{M}_{\ell\pm}$ $(E_{\ell\pm}, M_{\ell\pm})$ are assumed to have a Breit-Wigner energy dependence of the following form:

$$t^{\alpha,BW}_{\gamma,\eta}(W) = \mathcal{M}_{\ell\pm}(W) = \bar{\mathcal{M}}_{\ell\pm}\, f_{\gamma N}(W)\, \frac{M_R \Gamma_{\rm tot}(W)}{M_R^2 - W^2 - iM_R\Gamma_{\rm tot}(W)}\, f_{\eta N}(W)\, C_{\eta N}, \tag{34}$$

where $f_{\eta N}(W)$ is the usual Breit-Wigner factor describing the ηN decay of the N^* resonance with total energy dependent width $\Gamma_{\rm tot}(W)$, partial width $\Gamma_{\eta N}(W)$ and spin J,

$$f_{\eta N}(W) = \zeta_{\eta N} \left[\frac{1}{(2J+1)\pi}\, \frac{k(W)}{q_\eta(W)}\, \frac{M_N}{M_R}\, \frac{\Gamma_{\eta N}(W)}{\Gamma_{\rm tot}(W)^2} \right]^{1/2}, \tag{35}$$

with k and $q_\eta = q$ the photon and η meson momenta in the c.m. system, and $\zeta_{\eta N} = \pm 1$ a relative sign between the $N^* \to \eta N$ and $N^* \to \pi N$ couplings. $C_{\eta N}$ is an isospin factor, which is -1 for ηN and $\eta' N$ final states in the conventions used in our work.

For the total widths of the resonances, we assume up to seven decay channels, πN, $\pi\pi N$, ηN, $K\Lambda$, $K\Sigma$, ωN, and $\eta' N$,

$$\Gamma_{\rm tot}(W) = \Gamma_{\pi N}(W) + \Gamma_{\pi\pi N}(W) + \Gamma_{\eta N}(W) + \cdots . \tag{36}$$

The threshold energies for the decays are listed in table 1.

The energy dependence of the partial widths are given by

$$\Gamma_{\pi N}(W) = \beta_{\pi N}\, \Gamma_R \left(\frac{q_\pi(W)}{q_{\pi,R}}\right)^{2\ell+1} \left(\frac{X^2 + q^2_{\pi,R}}{X^2 + q_\pi(W)^2}\right)^{\ell}, \tag{37}$$

$$\Gamma_{\eta N}(W) = \beta_{\eta N}\, \Gamma_R \left(\frac{q_\eta(W)}{q_{\eta,R}}\right)^{2\ell+1} \left(\frac{X^2 + q^2_{\eta,R}}{X^2 + q_\eta(W)^2}\right)^{\ell}, \tag{38}$$

$$\Gamma_{\pi\pi N}(W) = \beta_{\pi\pi N}\, \Gamma_R \left(\frac{q_{2\pi}(W)}{q_{2\pi,R}}\right)^{2\ell+5} \left(\frac{X^2 + q^2_{2\pi,R}}{X^2 + q_{2\pi}(W)^2}\right)^{\ell+2}, \tag{39}$$

where X is a cut-off parameter, which has been fixed in the present work to $X = 450\,$MeV. The c.m. momenta of pion and eta are denoted by q_π and q_η, for the effective 2π channel we use a mass of $2m_\pi$. All momenta, taken at the resonance position, $W = M_R$, are denoted by an additional index R. All other 2-body channels are parameterized similarly as for πN or ηN. In general the dynamics of 3-body decays as for the $\pi\pi N$ channel are rather complicated and have most extensively been studied in the Jülich model. For single meson photoproduction the effective 2-body treatment works very well.

For the energy dependence of the photon vertex, we assume the form

$$f_{\gamma N}(W) = \left(\frac{k(W)}{k_R}\right)^2 \left(\frac{X_\gamma^2 + k_R^2}{X_\gamma^2 + k(W)^2}\right)^2, \tag{40}$$

with the photon c.m. momentum k, which takes the value k_R at the resonance position. In EtaMAID2018 we found best fits for $X_\gamma = 0$, and therefore, $f_{\gamma N} = 1$.

The so-called reduced multipoles $\bar{\mathcal{M}}_{\ell\pm}$ are related to the photon decay amplitudes $A_{1/2}$ and $A_{3/2}$ by

$$\bar{M}_{\ell+} = -\frac{1}{\ell+1}\left(A^{\ell+}_{1/2} + \sqrt{\frac{\ell+2}{\ell}}\, A^{\ell+}_{3/2}\right), \tag{41}$$

$$\bar{E}_{\ell+} = -\frac{1}{\ell+1}\left(A^{\ell+}_{1/2} - \sqrt{\frac{\ell}{\ell+2}}\, A^{\ell+}_{3/2}\right), \tag{42}$$

$$\bar{M}_{\ell+1,-} = +\frac{1}{\ell+1}\left(A^{\ell+1,-}_{1/2} - \sqrt{\frac{\ell}{\ell+2}}\, A^{\ell+1,-}_{3/2}\right), \tag{43}$$

$$\bar{E}_{\ell+1,-} = -\frac{1}{\ell+1}\left(A^{\ell+1,-}_{1/2} + \sqrt{\frac{\ell+2}{\ell}}\, A^{\ell+1,-}_{3/2}\right). \tag{44}$$

For specific resonances, see table 2.

So far we assumed that the resonance mass M_R is above all considered decay channels. However, as nucleon resonances obtain decay widths of the order of 100 MeV and more, also excitations of resonances are very likely, if the nominal Breit-Wigner mass is only a few MeV below threshold. But even for the Roper resonance, which

Table 2. The reduced multipoles $\bar{\mathcal{M}}_\alpha$ in terms of the photon decay amplitudes A_λ.

N^*	$\bar{E}$	$\bar{M}$
S_{11}	$-A_{1/2}$	–
P_{11}	–	$A_{1/2}$
P_{13}	$\frac{1}{2}(\frac{1}{\sqrt{3}}A_{3/2} - A_{1/2})$	$-\frac{1}{2}(\sqrt{3}A_{3/2} + A_{1/2})$
D_{13}	$-\frac{1}{2}(\sqrt{3}A_{3/2} + A_{1/2})$	$-\frac{1}{2}(\frac{1}{\sqrt{3}}A_{3/2} - A_{1/2})$
D_{15}	$\frac{1}{3}(\frac{1}{\sqrt{2}}A_{3/2} - A_{1/2})$	$-\frac{1}{3}(\sqrt{2}A_{3/2} + A_{1/2})$
F_{15}	$-\frac{1}{3}(\sqrt{2}A_{3/2} + A_{1/2})$	$-\frac{1}{3}(\frac{1}{\sqrt{2}}A_{3/2} - A_{1/2})$
F_{17}	$\frac{1}{4}(\sqrt{\frac{3}{5}}A_{3/2} - A_{1/2})$	$-\frac{1}{4}(\sqrt{\frac{5}{3}}A_{3/2} + A_{1/2})$
G_{17}	$-\frac{1}{4}(\sqrt{\frac{5}{3}}A_{3/2} + A_{1/2})$	$-\frac{1}{4}(\sqrt{\frac{3}{5}}A_{3/2} - A_{1/2})$
G_{19}	$\frac{1}{5}(\sqrt{\frac{2}{3}}A_{3/2} - A_{1/2})$	$-\frac{1}{5}(\sqrt{\frac{3}{2}}A_{3/2} + A_{1/2})$

is about 50 MeV below ηN threshold, an excitation in η photoproduction can be considered due to the large width of 350 MeV.

In such a case, however, the c.m. momentum $q_{a,R}$, which appears in the parametrization of the partial width $\Gamma_a(W)$, is no longer defined. In fact, one can analytically continue the momenta below zero and obtains imaginary values.

In the literature, two different methods are discussed. The first one takes a sharp cut-off with a θ-function, giving a zero value for the partial width below threshold. This is our EtaMAID approach. The second one (Flatte's approach [57]) uses the analytical continuation of the momentum below threshold and accepts the imaginary contribution of the width as a physical contribution to the mass.

For both methods we can generalize the parametrization of a partial width for arbitrary resonance masses

$$\Gamma_a(W) = g_a^2\, q_a(W) \left(\frac{|q_a^2(W)|}{X^2 + |q_a^2(W)|} \right)^\ell . \tag{45}$$

The squared momenta $q_a^2(W)$ become negative below threshold and could even produce singularities on the real axis in the physical region. Therefore, we take the absolute values.

For resonances with masses larger than $W_{a,thr}$ this form can be compared with the previous one, *e.g.* eq. (37), and this gives the relation between the coupling constants g_a and the branching ratios β_a,

$$\beta_a = \frac{g_a^2\, q_a(M_R)}{\Gamma_R\,(1 + X^2/q_a^2(M_R))^\ell} , \tag{46}$$

$$g_a^2 = \frac{\beta_a\, \Gamma_R}{q_a(M_R)}\,(1 + X^2/q_a^2(M_R))^\ell . \tag{47}$$

For the 3-body 2π channel we also make a small adjustment,

$$\Gamma_{\pi\pi}(W) = g_{\pi\pi}^2\, q_{2\pi}(W) \left(\frac{q_{2\pi}^2(W)}{X^2 + q_{2\pi}^2(W)} \right)^{\ell+2} , \tag{48}$$

however, with a slightly different asymptotic behavior compared to eq. (39).

For both πN and $\pi\pi N$ channels, all nucleon resonances are above threshold and the conventional definition of branching ratios can be used. For ηN only the Roper resonance $N(1440)\frac{1}{2}^+$ is below threshold. In the $K\Sigma$ channel $N(1650)\frac{1}{2}^-$ and in the ωN channel $N(1710)\frac{1}{2}^+$ are below threshold but with large couplings that make significant contributions above threshold. Finally, in the $\eta' N$ channel we even find four states below threshold, see table 5 in appendix C.

4 Results

4.1 Data base

In our analysis we only use modern data which cover a broad energy and angular range. We prefer datasets with smallest statistical uncertainties and we only combine data from different experiments if they are in agreement in overlapping energy regions without including additional scaling parameters. The unpolarized differential cross section has been measured with by far highest accuracy at MAMI. From several datasets we use those with the most sophisticated reconstruction and error analysis [58]. The energy range of MAMI is limited to $W < 1970$ MeV. We used the differential cross section from the CLAS Collaboration [59] in this fit because of their much smaller statistical errors, larger energy coverage, and better agreement with the high statistics data from A2MAMI [58] in an overlapping energy region than CBELSA/TAPS data [8]. The angular-dependent systematic uncertainty for results of Run-I and Run-II above $W = 1796$ MeV was evaluated as 3%, for Run-III and for the η' differential cross sections as 5–6%. These uncertainties were added in quadrature to the statistical uncertainties [58]. For other data, we use only statistical uncertainties in the fit.

The photon beam asymmetry Σ has been measured over the full resonance region by GRAAL and CLAS. We include all polarized target and beam-target asymmetries from modern experiments. Old data, in particular an early target asymmetry measurement at ELSA [60], cannot compete with regard to statistical and systematic uncertainties and are not used in our analysis.

The differential cross sections cover the energy region from threshold up to $W = 2.8$ GeV. Polarization observables are from threshold up to $W = 1.85$ GeV for T and F, up to $W = 2.13$ GeV for E, and up to $W = 2.08$ GeV for Σ. These are five polarization observables for the ηp channel with good energy and angular coverage, which is however, still far away from a complete experiment, that would require at least 8 observables including those with

Table 3. Experimental data on η and η' photoproduction. The column "used" shows the data that were included in our fits and those that were ignored. N is the number of data points and χ^2 is the total weighted deviation from our standard 2018 solution for that dataset.

Observable	Reaction	Used	W [MeV]	N	χ^2	χ^2/N	Reference
σ_0	$p(\gamma,\eta)p$	–	1488–1870	2880	9502	3.3	A2MAMI-17 (Run I) [58]
σ_0	$p(\gamma,\eta)p$	$\surd$	1488–1891	2712	4437	1.6	A2MAMI-17 (Run II) [58]
σ_0	$p(\gamma,\eta)p$	$\surd$	1888–1957	288	329	1.1	A2MAMI-17 (Run III) [58]
σ_0	$p(\gamma,\eta)p$	$\surd$	1965–2795	634	2276	3.6	CLAS-09 [59]
σ_0	$p(\gamma,\eta)p$	–	1588–2370	680	8640	13.	CBELSA/TAPS-09 [8]
Σ	$p(\gamma,\eta)p$	$\surd$	1496–1908	150	394	2.6	GRAAL-07 [61]
Σ	$p(\gamma,\eta)p$	$\surd$	1700–2080	214	617	2.9	CLAS-17 [62]
T	$p(\gamma,\eta)p$	$\surd$	1497–1848	144	246	1.7	A2MAMI-14 [63]
F	$p(\gamma,\eta)p$	$\surd$	1497–1848	144	246	1.7	A2MAMI-14 [63]
E	$p(\gamma,\eta)p$	$\surd$	1525–2125	73	155	2.1	CLAS-16 [64]
E	$p(\gamma,\eta)p$	$\surd$	1505–1882	135	255	1.9	A2MAMI-17 [65,66]
σ_0	$n(\gamma,\eta)n$	$\surd$	1492–1875	880	3079	3.5	A2MAMI-14 [67]
σ_0	$n(\gamma,\eta)n$	–	1505–2181	322	2986	9.3	CBELSA/TAPS-11 [68]
σ_0	$n(\gamma,\eta)n$	–	1588–2070	317	4992	16.	CBELSA/TAPS-17 [69]
Σ	$n(\gamma,\eta)n$	$\surd$	1504–1892	99	177	1.8	GRAAL-08 [70]
E	$n(\gamma,\eta)n$	$\surd$	1505–1882	135	209	1.5	A2MAMI-17 [65,66]
σ_0	$p(\gamma,\eta')p$	$\surd$	1898–1956	120	198	1.7	A2MAMI-17 [58]
σ_0	$p(\gamma,\eta')p$	$\surd$	1925–2795	681	2013	3.0	CLAS-09 [59]
σ_0	$p(\gamma,\eta')p$	–	1934–2351	200	278	1.4	CBELSA/TAPS-09 [8]
Σ	$p(\gamma,\eta')p$	$\surd$	1903–1913	14	35	2.5	GRAAL-15 [71]
Σ	$p(\gamma,\eta')p$	$\surd$	1904–2080	62	85	1.4	CLAS-17 [62]
σ_0	$n(\gamma,\eta')n$	$\surd$	1936–2342	170	191	1.1	CBELSA/TAPS-11 [72]

recoil polarization detection. Therefore, some ambiguities in the PWA can be expected.

Data sets for the other reactions are much more scarce than for $\gamma p \to \eta p$. In the ηn channel we have only three observables, for $\eta' p$ two and for $\eta' n$ just the differential cross section alone, see table 3.

In our fits to the data we have used a total of 208 parameters. For the resonance sector with 21 N^* resonances we have 112 parameters for BW parametrization and 66 for unitarity phases. The background is described with 20 parameters, mainly for the Regge parametrization.

4.2 Total cross sections

We begin the discussions of our results with the total cross sections of the four channels considered in our work: $p(\gamma,\eta)p$, $n(\gamma,\eta)n$, $p(\gamma,\eta')p$, $n(\gamma,\eta')n$.

The data in figs. 4–10 are from A2 Collaboration at MAMI: A2MAMI-17 [58] and A2MAMI-14 [67]; CBELSA/TAPS Collaboration: CBELSA/TAPS-09 [8], CBELSA/TAPS-11 for ηn [68] and for $\eta' n$ [72], and CBELSA/TAPS-17 [69]. In the case of the CLAS-09 data, we show data points that were obtained in a Legendre fit to the differential cross sections from CLAS Collaboration [59] and are affected by additional uncertainties due to a limited angular range of the data especially in forward direction. The total cross section data shown here have not been used in our fit, only the differential cross sections were fitted.

The fit results for the total cross sections are presented in fig. 4 together with corresponding experimental data.

In fig. 4(a), there are very interesting features visible at energies $W \approx 1680\,\text{MeV}$ and $W \approx 1890\,\text{MeV}$, which can be explained by cusp effects due to the opening of new strong channels in the S-wave.

The cusp in the ηp total cross section, in connection with the steep rise of the $\eta' p$ from its threshold, fig. 4(b), is explained by a strong coupling of the $S_{11}(1895)$ resonance to both channels, see also figs. 5, 6. Unfortunately, there are no data for the $\eta' n$ channel near threshold and only one data point exists in the cusp region for the ηn channel, fig. 4(a). Nevertheless our solution demonstrates also a strong coupling of the $S_{11}(1895)$ for these neutron channels.

Other interesting structures are observed as a dip in $\gamma p \to \eta p$ and a bump in $\gamma n \to \eta n$ around $W \approx 1680\,\text{MeV}$,

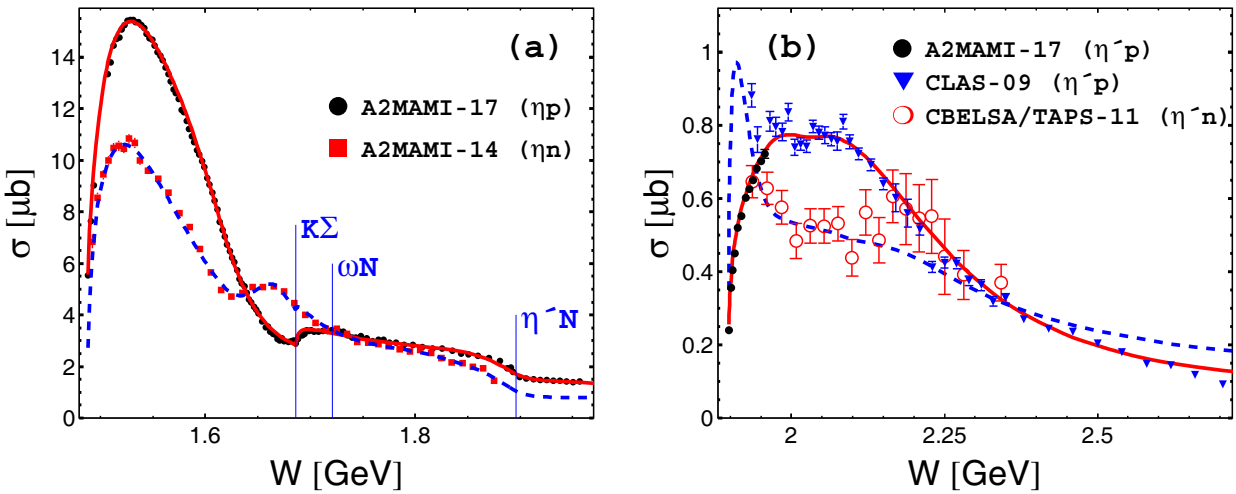

Fig. 4. Total cross section for (γ, η) (a) and (γ, η') (b) on protons and neutrons. The solid red and dashed blue lines show our EtaMAID solution for proton and neutron, respectively.

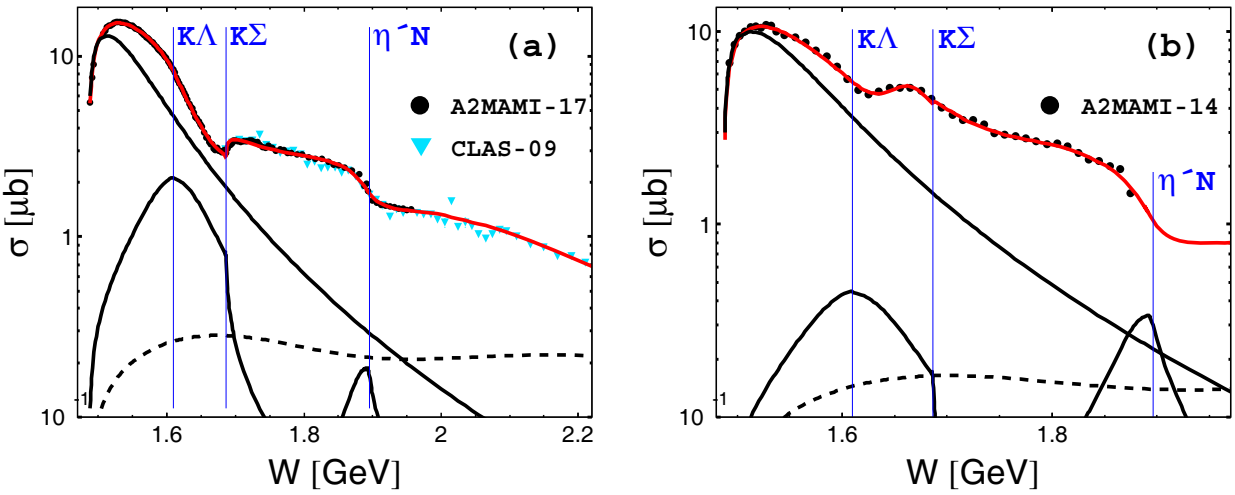

Fig. 5. Partial contributions of the S-wave resonances to the total cross section for (γ, η) on protons (a) and neutrons (b) in comparison with the non-resonant background. The solid red lines show our full EtaMAID solution. The individual contribution of $S_{11}(1535)$, $S_{11}(1650)$ and $S_{11}(1895)$ resonances are shown by solid black lines. The dashed line shows the total background of Born and Regge contributions including the damping factors. Vertical lines correspond to thresholds of $K\Lambda$, $K\Sigma$, and $\eta' N$ photoproduction.

fig. 4(a). Both structures were observed experimentally many times and its existence is unambiguous. However its nature is not yet fully understood. See for more details ref. [2]. Our analysis shows that the narrow bump in ηn and the dip in ηp channels have different origin. The first is a result of an interference of few resonances with a dominant contribution of the $P_{11}(1710)$, see fig. 5(b) and fig. 6(b). The second one is mainly a sum of $S_{11}(1535)$ and $S_{11}(1650)$ with opposite signs. However the narrowness of this structure is explained by a cusp effect due to the opening of the $K\Sigma$ decay channel of the $S_{11}(1650)$ resonance, see fig. 5(a) and fig. 6(a).

In fig. 5–7 we show partial resonance contributions for η and η' photoproduction in four channels. In fig. 5 we concentrate on the most important S_{11} resonances $N(1535)\frac{1}{2}^-$, $N(1650)\frac{1}{2}^-$ and $N(1895)\frac{1}{2}^-$. The $S_{11}(1535)$ completely dominates both proton and neutron channels. And, as a side remark, due to the large branchings into the πN and ηN channels, this resonance produces a very significant cusp effect in the cross sections of pion photoproduction [73,74]. The second $S_{11}(1650)$ exhibits visible cusp effects due to the opening of the $K\Lambda$ and $K\Sigma$ channels. Also the third $S_{11}(1895)$ shows a visible cusp at $\eta' N$ threshold. In the full solution the $K\Lambda$ cusp remains hidden under the strong $S_{11}(1535)$ contribution, also the $K\Sigma$ cusp becomes invisible in the neutron channel. But in the proton channel this cusp appears as a very pronounced dip with even a kind of a bump afterwards. The $\eta' N$ cusps due to the third $S_{11}(1895)$ resonance are visible in both proton and neutron channels, and in case of the proton the cusp is very well supported by the high-precision data of A2-MAMI.

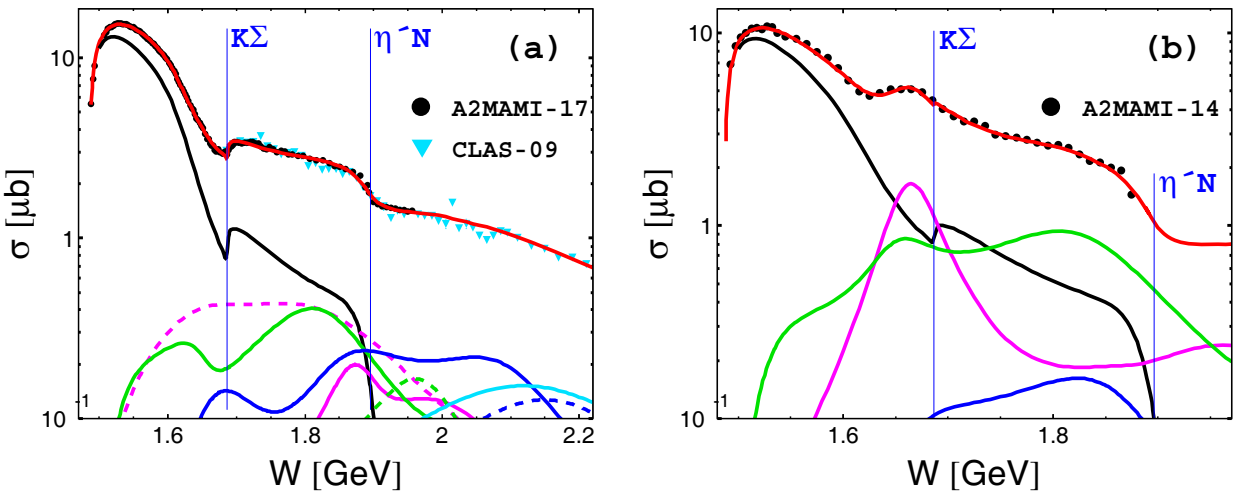

Fig. 6. Resonance contributions of partial waves to the total cross section for (γ, η) on protons (a) and neutrons (b). The solid red lines show our full EtaMAID solution including background. The black solid lines are the sum of three $S_{11}(1535, 1650, 1895)$ resonances, magenta solid: four $P_{11}(1440, 1710, 1880, 2100)$, magenta dashed: two $P_{13}(1720, 1900)$, green solid: four $D_{13}(1520, 1700, 1875, 2120)$, green dashed: two $D_{15}(1675, 2060)$, blue solid: three $F_{15}(1680, 1860, 2000)$, blue dashed: $F_{17}(1990)$ and cyan solid: $G_{17}(2190)$. Vertical lines correspond to thresholds of $K\Sigma$ and $\eta' N$ photoproduction.

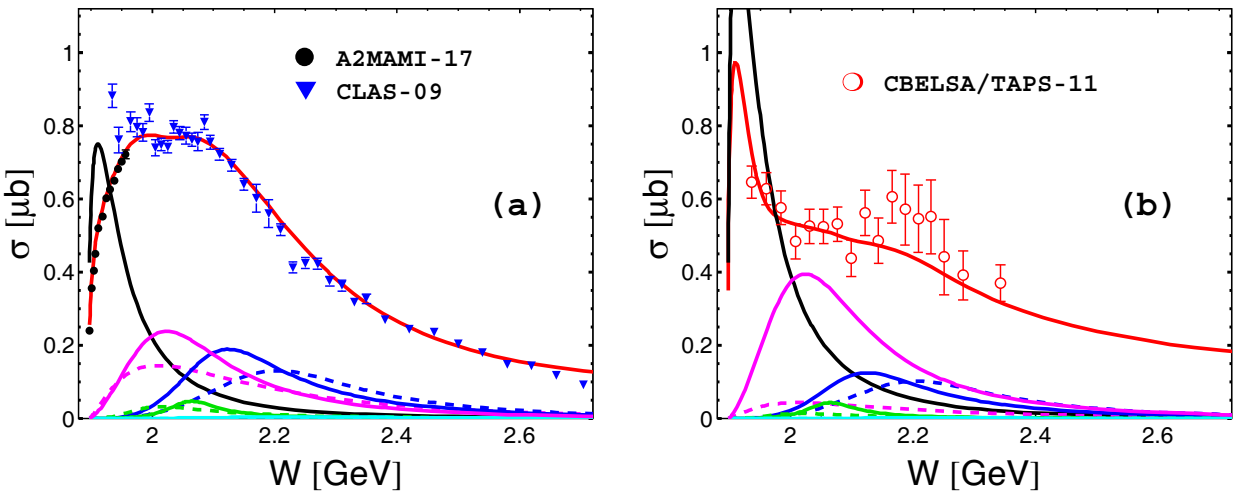

Fig. 7. Partial contributions of the resonances to the total cross section for (γ, η') on protons (a) and neutrons (b). The solid red lines show our full EtaMAID solution. The other curves show resonance contributions of $S_{11}(1895)$: black solid, $P_{11}(1880, 2100)$: magenta solid, $P_{13}(1900)$: magenta dashed, $D_{13}(1875)$: green solid, $D_{15}(2000)$: green dashed, $F_{15}(2000)$: blue solid, and $F_{17}(1990)$: blue dashed.

The cusp structures are even better visible in fig. 6, where all resonances within the same partial wave are summed up. In the cases of P_{11} and D_{13} these are sums over even four N^* resonances. From this figure it becomes very clear that the bump structures at $W \approx 1680\,\text{MeV}$ is a cusp effect of the $S_{11}(1650)$ in the proton channel and a resonance effect of the $P_{11}(1710)$ in the neutron channel.

The largest N^* resonance contributions in (γ, η) total cross sections are from $S_{11}(1535, 1650, 1895)$, $P_{11}(1710)$, $P_{13}(1720, 1900)$, and $D_{13}(1700, 1875)$.

Figure 7 shows the partial contributions of the N^* resonances to the total cross sections for (γ, η') on proton and neutron. The largest resonance contributions in the total cross sections for (γ, η') are from $S_{11}(1895)$, $P_{11}(1880)$, $P_{11}(2100)$, $F_{15}(2000)$ and $F_{17}(1990)$. It is interesting to note, that the first two of them have Breit-Wigner masses below threshold but appear as resonance bumps above threshold due to phase space factors.

In both channels the S_{11} resonance dominates near threshold and the second largest peak arises from P_{11}, followed by large contributions from F-wave resonances. This is different in the most recent BnGa analysis [34], where the $P_{13}(1900)$ plays a dominant role and F-waves are practically negligible. Such ambiguities in the PWA can be expected when only two observables are measured as in the η' proton channel. For the neutron channel, there is even only the differential cross section measured. Such an incompleteness in the polarization observables

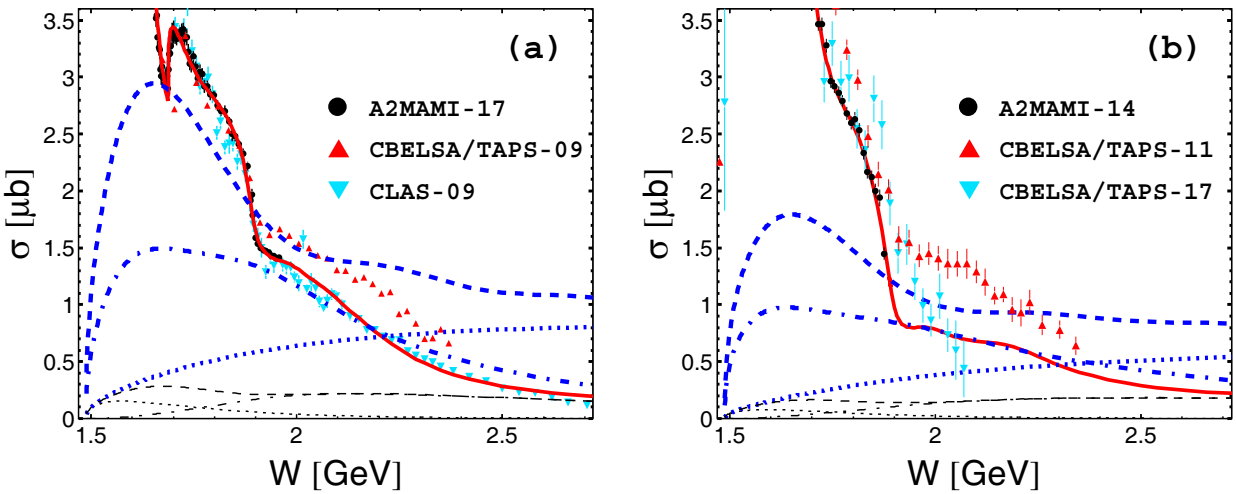

Fig. 8. Partial contributions of the background to the total cross section for (γ, η) on protons (a) and neutrons (b). The solid red lines show our full EtaMAID solution. The wide blue dotted, dash-dotted, and dashed lines show Born, Regge, and Born+Regge, respectively, without damping factors. The thin black dotted, dash-dotted, and dashed lines show the same, when damping factors are applied. The CBELSA/TAPS data have not been used in our fit.

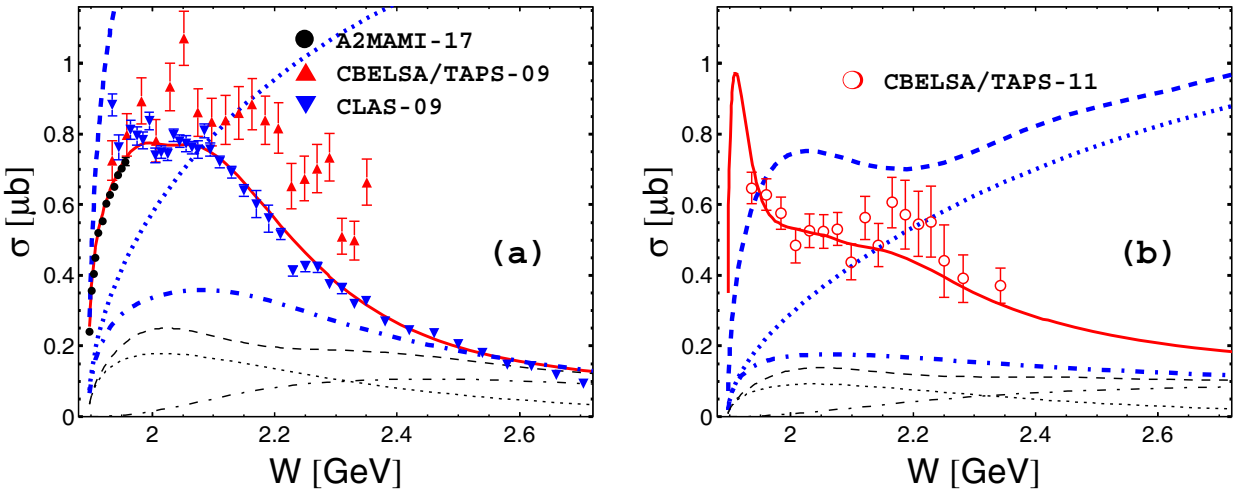

Fig. 9. Partial contributions of the background to the total cross section for (γ, η') on protons (a) and neutrons (b). Notation of curves is as in fig. 8.

naturally leads to large ambiguities in the partial wave analysis.

In fig. 8 and fig. 9 we show the background contributions for η and η' photoproduction in four channels. The blue dotted, dash-dotted and dashed lines are obtained by Born terms, t-channel vector meson exchanges in Regge parametrization and the sum of both, respectively. The Born terms rise very strongly already near threshold in η' photoproduction and appear also very large in η photoproduction for energies above 2 GeV. The t-channel Regge contributions are also quite large in the resonance region below 2.5 GeV and dominate the cross section for energies above 2 GeV. The double counting of Regge and resonances becomes quite obvious. Therefore, as explained in sect. 3 before, we have introduced damping factors for the background contributions, eqs. (18) and (30), yielding to the black dotted, dash-dotted and dashed lines for Born, Regge and total background, respectively.

Finally, in fig. 10 we compare our EtaMAID2018 solution with the new 2018 updates of Bonn-Gatchina (BnGa) [35], Jülich-Bonn (JüBo) [36] and Kent State University (KSU) [37].

While EtaMAID has analyzed all four channels up to $W = 4.5$ GeV ($E \approx 10$ GeV), BnGa analyzed three, ηp, ηn, and $\eta' p$ up to $W = 2.5$ GeV, KSU analyzed two, ηp up to $W = 2.0$ GeV and ηn up to $W = 1.9$ GeV and JüBo analyzed only the ηp channel up to $W = 2.4$ GeV. JüBo and KSU, which did not include the latest A2MAMI-17 data, differ significantly from the data in the dip region around $W \approx 1680$ MeV and around the η' threshold, the BnGa solution describes the data much better. The best description of the data is obtained with EtaMAID.

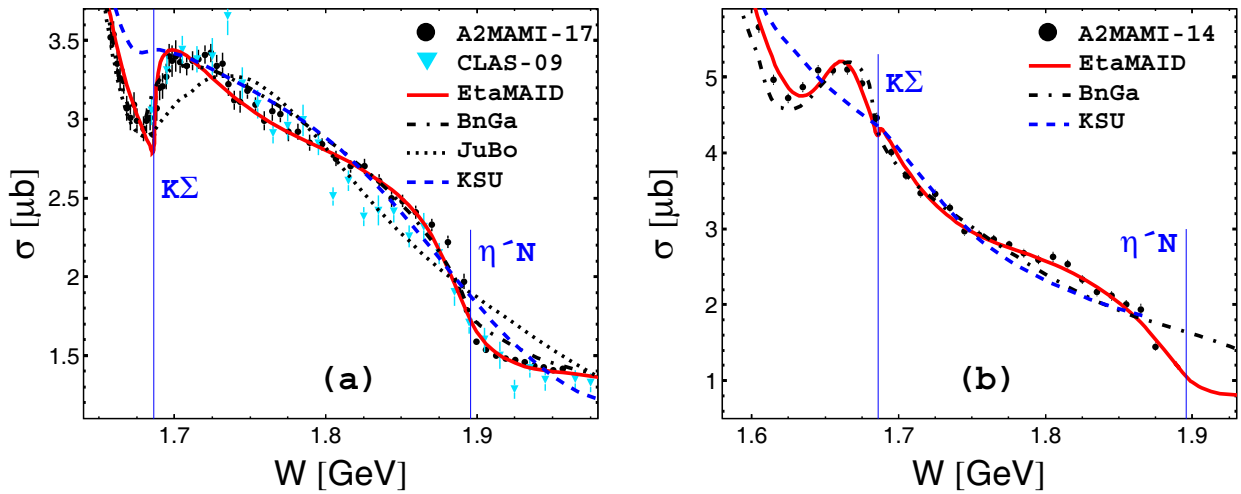

Fig. 10. Total cross section for (γ, η) on protons (a) and neutrons (b) in comparison with other newly updated PWA. The solid red lines show our full EtaMAID solution. The black dash-dotted, dotted and blue dashed curves are obtained from the newly updated BnGa [35], JüBo [36] and KSU [37] partial wave analyses. Near η threshold, below 1.6 GeV, all solutions are practically identical. Vertical lines correspond to thresholds of $K\Sigma$, and $\eta' N$ photoproduction.

Table 4. Breit-Wigner parameters for selected resonances: mass M_{BW}, total width Γ_{BW}, branching ratio $\beta_{\eta N}$ to ηN, and helicity amplitudes $A^{p(n)}_{1/2}$ for proton (neutron). The first row for each resonance gives a parameter set of the presented EtaMAID solution. The parameters indicated without errors were fixed during the fit. The second row indicate an overall status of the resonance and lists the corresponding parameters estimated by PDG [1] (NE means "No Estimates" given by PDG). The effective $\eta' N$ branching ratios according to ref. [75] for the $N(1880)1/2^+$ and $N(1895)1/2^-$ are $(6.3 \pm 2)\%$ and $(19.5 \pm 5)\%$, respectively.

Resonance J^P	M_{BW} [MeV]	Γ_{BW} [MeV]	$\beta_{\eta N}$ [%]	$A^p_{1/2}$ [10^{-3} GeV$^{-1/2}$]	$A^n_{1/2}$ [10^{-3} GeV$^{-1/2}$]
$N(1535)1/2^-$	1522 ± 8	175 ± 25	34 ± 5	$+115$	-102 ± 8
$****$	1530 ± 15	150 ± 25	42 ± 13	$+105 \pm 15$	-75 ± 20
$N(1650)1/2^-$	1626^{+10}_{-5}	133 ± 20	19 ± 6	$+55$	-25 ± 20
$****$	1650 ± 15	125 ± 25	25 ± 10	$+45 \pm 10$	-10^{+40}_{-30}
$N(1710)1/2^+$	1670 ± 20	63^{+55}_{-18}	12 ± 4	5.5	-42^{+16}_{-12}
$****$	1710 ± 30	140 ± 60	30 ± 20	NE	NE
$N(1880)1/2^+$	1882 ± 24	90^{+70}_{-30}	43^{+10}_{-20}	60	-7^{+60}_{-60}
$***$	1880 ± 50	300 ± 100	NE	NE	NE
$N(1895)1/2^-$	1894.4^{+5}_{-15}	71^{+25}_{-13}	3.3 ± 1.5	-32	$+43^{+30}_{-50}$
$****$	1895 ± 25	120^{+80}_{-40}	25^{+15}_{-10}	NE	NE

In appendix C we list all background and resonance parameters of our model. For a few selected very important S_{11} and P_{11} resonances we also give an error analysis for Breit-Wigner parameters based on MINUIT-MINOS in table 4. We also have calculated effective $\eta' N$ branching ratios by integrating the decay spectrum above $\eta' N$ threshold according to ref. [75]. For the $N(1880)1/2^+$ and $N(1895)1/2^-$ we obtained $(6.3 \pm 2)\%$ and $(19.5 \pm 5)\%$, respectively. A complete resonance analysis, especially with pole positions and residues will be published in a following paper.

4.3 Comparison with the data of $d\sigma/d\Omega$, Σ, T, F, E for $\gamma\, p \to \eta\, p$

In this subsection we turn to differential cross sections and polarization observables for η production on the proton target. Figures 11–13 display the differential cross section for the reaction $\gamma p \to \eta p$ as a function of the cosine of the c.m. scattering angle in comparison with the full solution (solid red curves). We point out that our full solution provides an excellent description of the data over the whole energy and angular range, including the $K\Sigma$ and η' cusp regions, $W \approx 1680$ MeV and $W \approx 1890$ MeV, respectively.

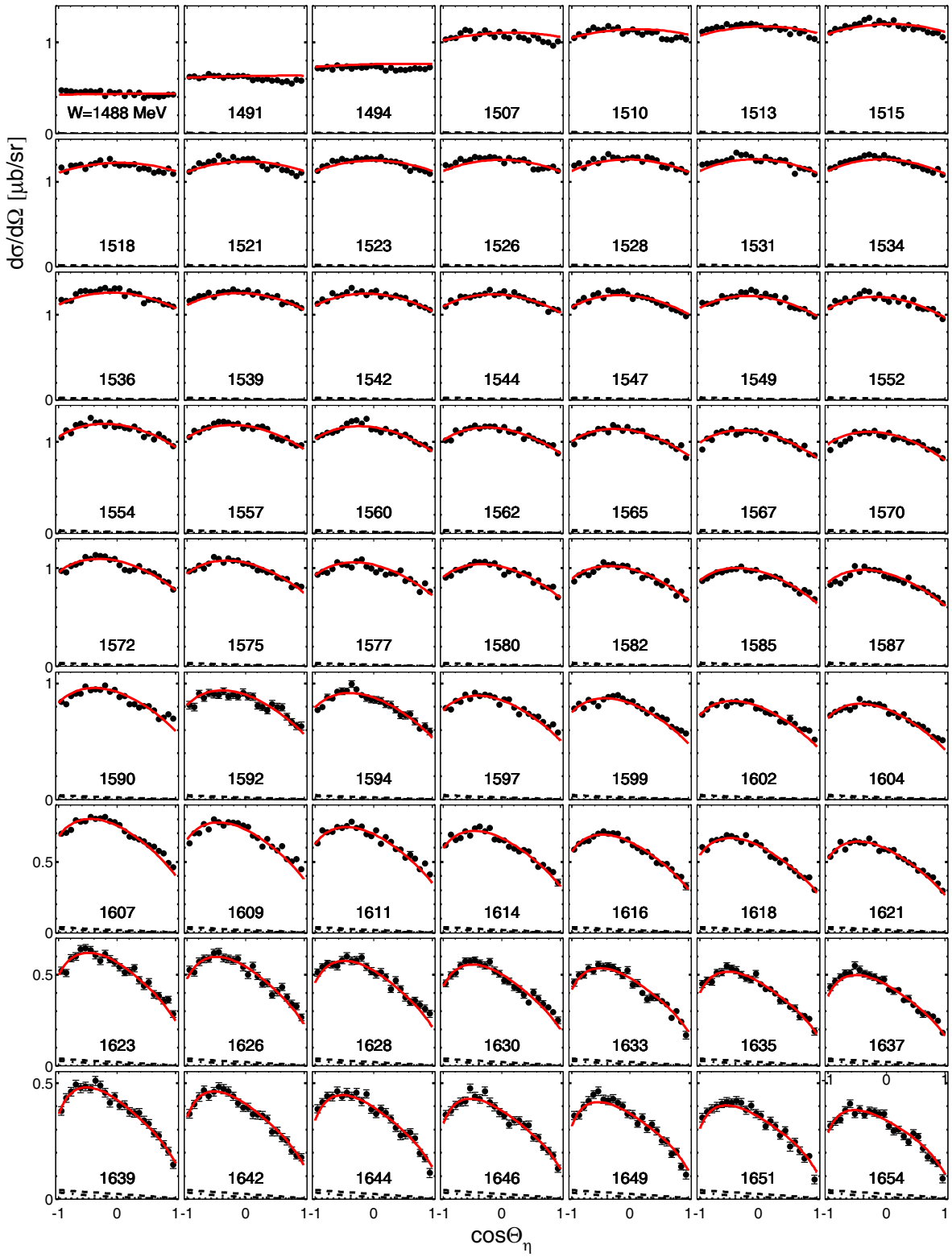

Fig. 11. Differential cross section for (γ, η) on the proton for $1488\,\text{MeV} \leq W \leq 1654\,\text{MeV}$ as function of cosine of the c.m. scattering angle. The solid red lines show our full solutions, whereas the black dotted, dash-dotted, and dashed lines are Born terms, Regge, and full background, respectively. The data are from A2MAMI [58].

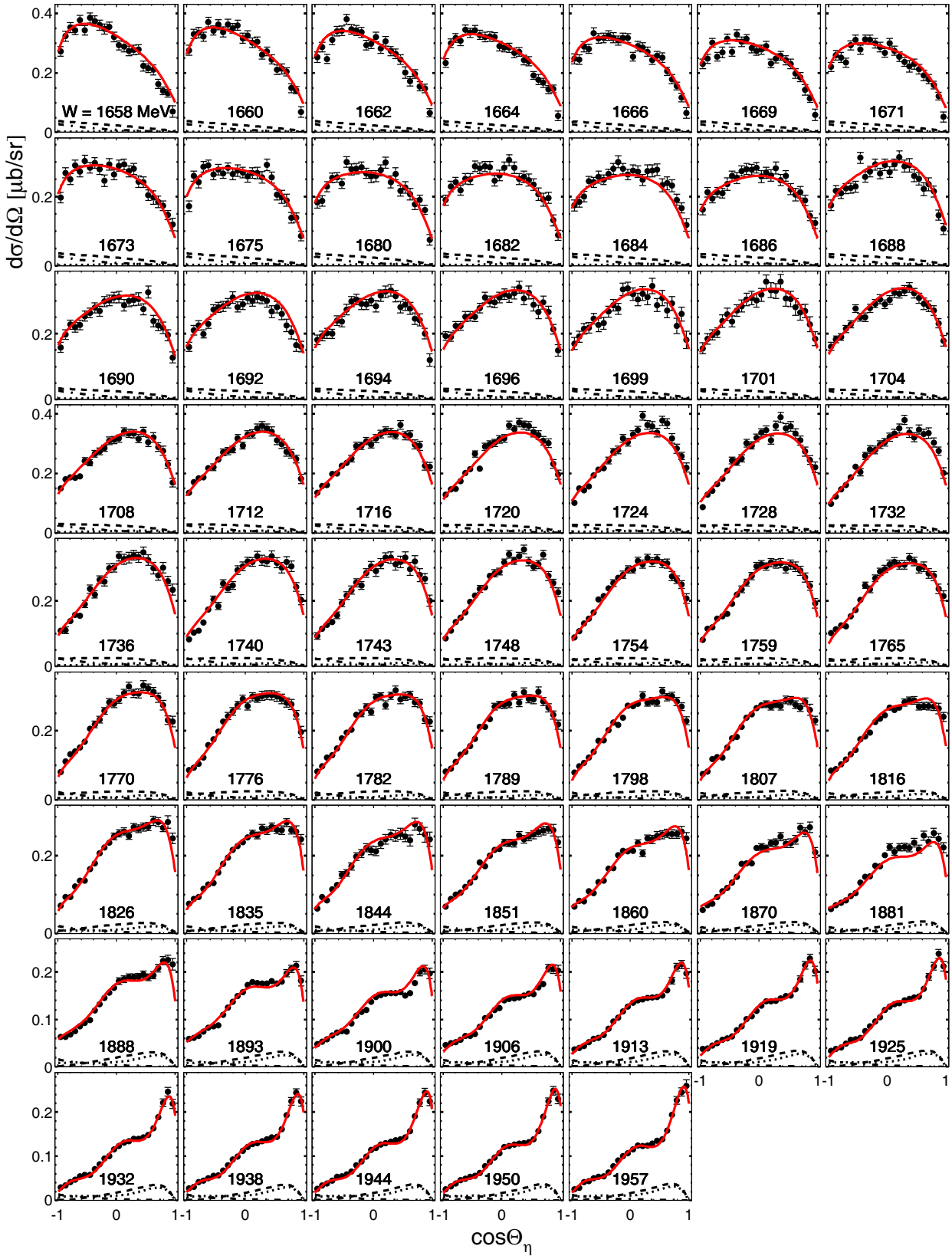

Fig. 12. Same as in fig. 11 for c.m. energies 1658 MeV $\leq W \leq$ 1957 MeV.

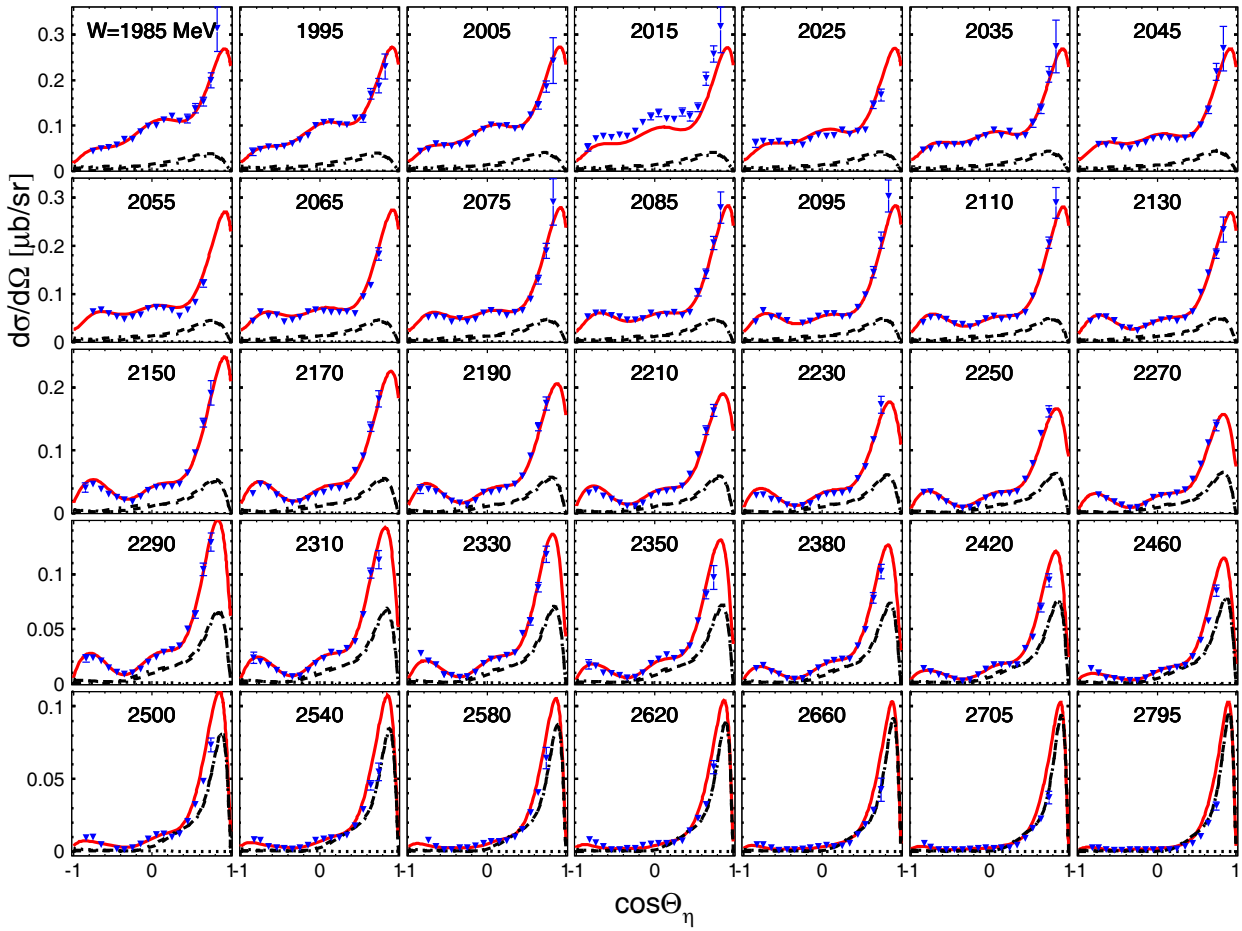

Fig. 13. Same as in fig. 11 for c.m. energies 1985 MeV $\leq W \leq$ 2795 MeV. The data are from CLAS [59].

It is informative to observe the impact of the background contributions, Born (dotted curves), Regge (dash-dotted), and Born + Regge (dashed) contributions. Throughout the whole energy range of MAMI data [58] and well into the CLAS [59] energy range, for $W \leq 2200$ MeV the background contributions are quite small, although background-resonance interference may be non-negligible. This observation is of importance to assess the issue of double counting mentioned in the introduction in view of using a modified Regge amplitude in the resonance region. We interpret the small relative impact of the background amplitudes for $W \leq 2200$ MeV as an indication that double counting does not pose problems for those energies, and only the two highest resonances of our analysis, $N(2190)\frac{7}{2}^-$ and $N(2250)\frac{9}{2}^-$, may be severely affected by that problem. Above $W \approx 2500$ MeV the Regge contribution becomes dominant. We postpone a detailed study of the contribution of the modified Regge background to resonant partial waves in the transition region 2200 MeV $\leq W \leq$ 2500 MeV and extraction of higher resonance parameters to the upcoming work.

Polarization observables are much more critical tests for models than total and differential cross sections as they are sensitive to real and imaginary parts of interferences of amplitudes. Figure 14 shows a comparison of EtaMAID2018, BnGa, JüBo and KSU models to data on target polarization T and beam-target polarization F asymmetries from A2MAMI for 1497 MeV $\leq W \leq$ 1848 MeV as function of cosine of the c.m. scattering angle. It is seen that our solution describes the data nicely for all energies and in the full angular range, whereas other models show considerable deviations from data for $W \geq 1600$ MeV. We observe a significant spread between data points in some neighboring angular bins, so more precise and self-consistent data on this observable will help discriminating among the models.

In fig. 15, data on the photon beam asymmetry Σ from GRAAL [61] and CLAS [62] in comparison with models are shown. The two data sets show a disagreement in several energy bins in the overlap region 1700 MeV $\leq W \leq$ 1900 MeV which makes it difficult to judge the quality of the model description of the data. The JüBo model fails to reproduce the high quality GRAAL data at lower energies, especially at backward angles, while all other models describe that energy region successfully. At highest energies, this asymmetry shows a peculiar shape, peaks at forward and backward angles and a dip around 90°. Since EtaMAID2018, JüBo and BnGa models deviate somewhat

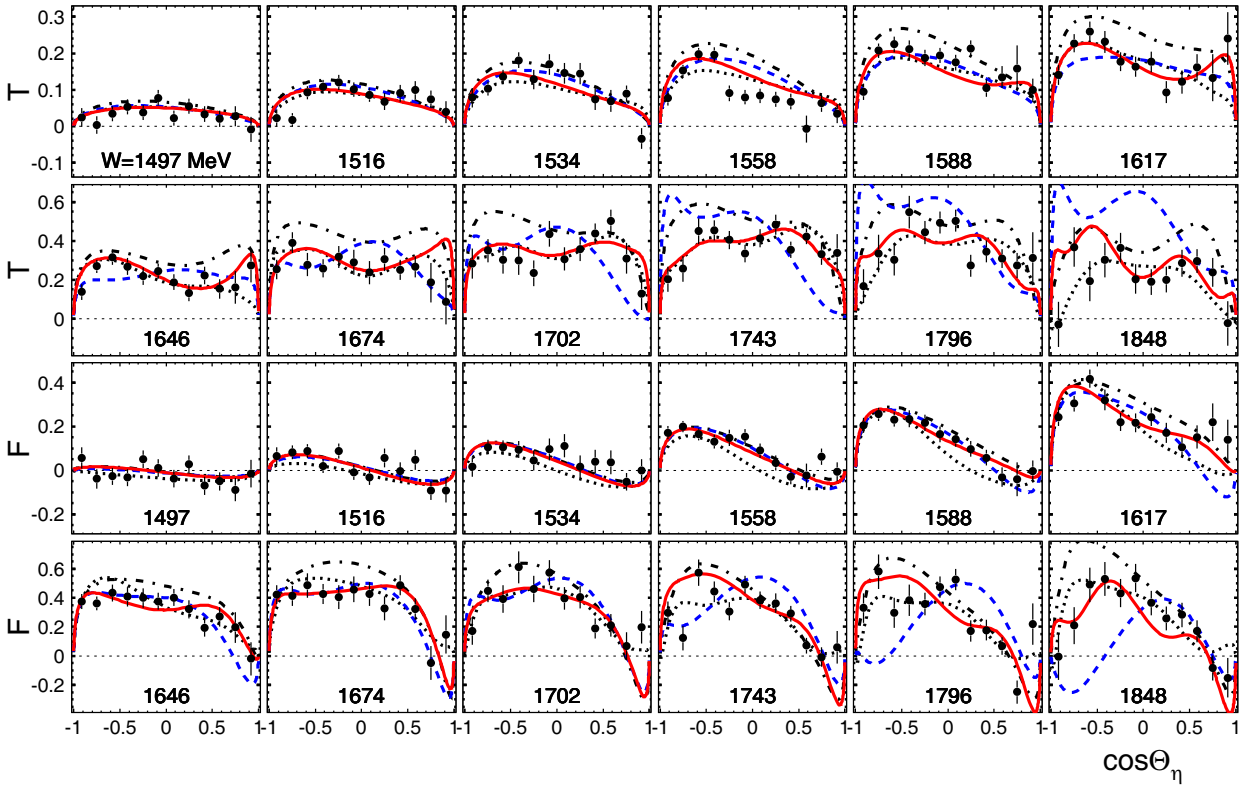

Fig. 14. Target polarization T (upper panels) and beam-target polarization F (lower panels) asymmetries for (γ, η) on the proton. The solid red lines show our full solution. Results of other PWA are shown by the black dash-dotted (BnGa [35]), the black dotted (JüBo [36]), and the blue dashed (KSU [37]) lines. The data points are from A2MAMI [63].

from each other, better statistics data on Σ at these energies will be helpful.

For the beam-target polarization asymmetry E, fig. 16, the situation is similar: All models give very similar results for $W \leq 1700$ MeV but start deviating above. The current quality of the data does not permit to draw firm conclusions from this comparison.

In view of this general sensitivity of polarization observables to models, in fig. 17 we plot predictions of the four models for the observables P, H, G, C_x, and C_z for (γ, η) on the proton, for which no data exist. All these observables look very promising for discriminating the models, especially at higher energies.

It is interesting to note that in some energy regions, the observables P and H are almost identical up to a sign. As can be seen from $P + H$, eq. (A.9) together with the multipole expansion, eq. (15), all S-wave contributions cancel exactly and the leading terms are imaginary parts of P-D interferences. In EtaMAID a sizable deviation between P and $-H$ is only seen at higher energies in fig. 17, while BnGa and JüBo exhibit larger differences.

4.4 Comparison with the data of $d\sigma/d\Omega$, Σ, E for $\gamma\, n \rightarrow \eta\, n$

Results for $\gamma\, n \rightarrow \eta\, n$ reaction are shown in figs. 18–20. Similarly to the proton target, we observe a very good description of the differential cross section data in the full energy range where very precise A2MAMI data are available, with the mere exception of some very backward or very forward (in the c.m. frame) data points at low energies where nuclear effects may lead to some systematic effects that were not fully accounted for [2]. This lack of strength in the extreme backward and forward kinematics is however not reflected in the description of the total cross section, see fig. 4.

Polarization observables Σ and E are shown in figs. 19 and 20, respectively. Our model describes the data nicely, although at present the uncertainties of the data do not allow for a definitive comparison of the models and will help to remove ambiguities, which are still visible in the partial wave analysis, see sect. 6.

In fig. 21 we plot the polarization observables P, H, G, T, and F for (γ, η) on the neutron. As for the proton target, data on these observables will yield a crucial test for our understanding of the models. As also discussed for the proton, the symmetry between the P and H observables is again much more pronounced for EtaMAID than for other solutions, a signature for a stronger S-wave dominance in EtaMAID.

4.5 Comparison with the data of $d\sigma/d\Omega$ and Σ for $\gamma\, p \rightarrow \eta'\, p$ and $\gamma\, n \rightarrow \eta'\, n$

Results for $\gamma\, p \rightarrow \eta'\, p$ are presented in figs. 22 and 23. For the differential cross sections, we show the impact

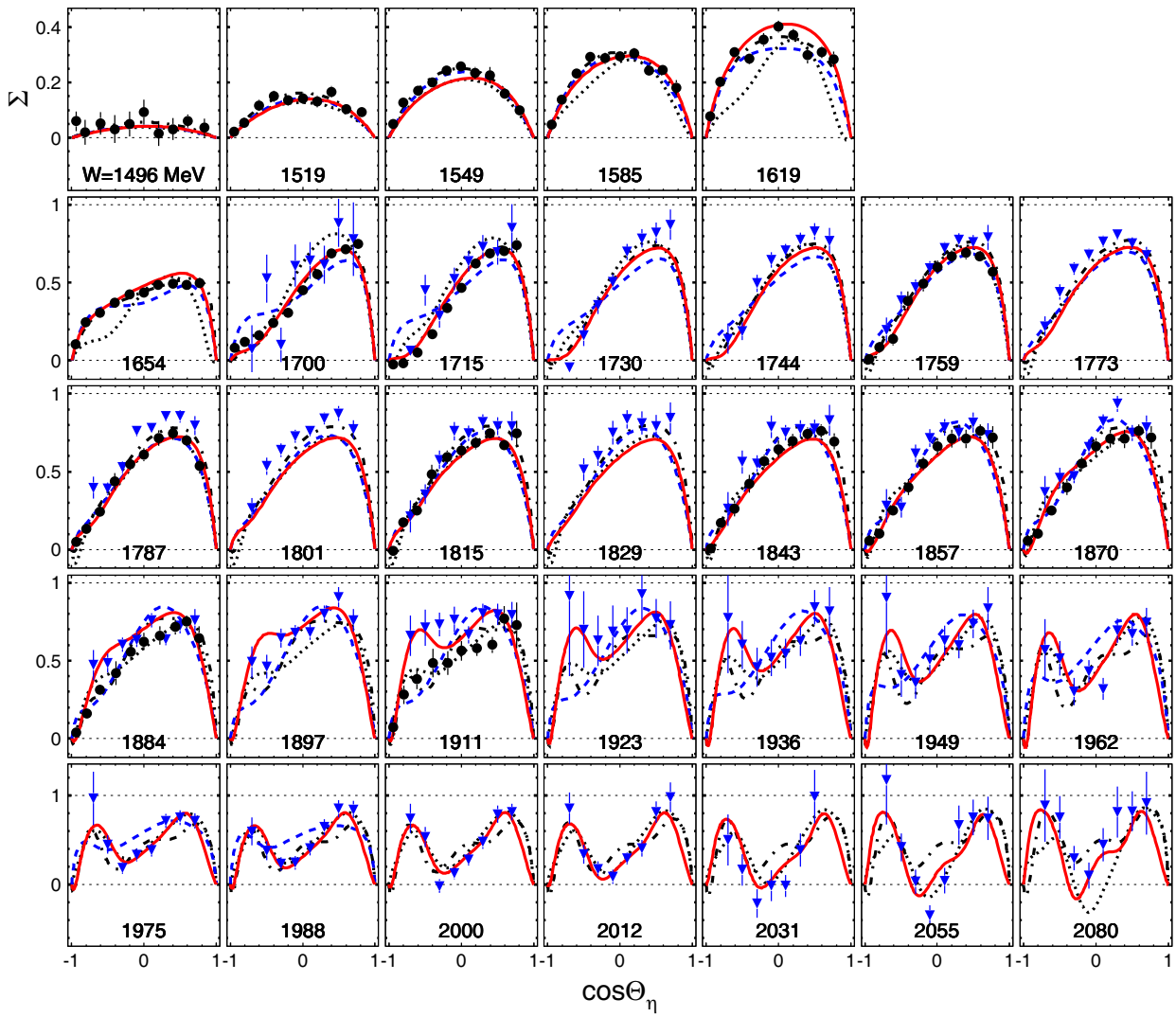

Fig. 15. Photon beam asymmetry Σ for (γ, η) on the proton. The black circles and blue triangles are data from GRAAL [61] and CLAS [62] respectively. Notation of the curves is as in fig. 14.

of the background contributions, Born (dotted), Regge (dash-dotted), and Born + Regge (dashed) contributions. Because of the higher threshold for η' production, the background has much more relative impact than for η production. In particular, we observe that the Born contribution, more precisely, the u-channel Born diagram, gives a very sizable contribution at backward angles for $W \geq 1912$ MeV. We note in this respect that a Reggeization of the u-channel nucleon exchange is worthwhile to study in the upcoming work. With this in mind, we notice a very good description of the data in the full energy and angular range by our solution. Apparent disagreement between A2MAMI and CLAS data, where the two data sets overlap, play little role at present due to a much better statistics of Mainz data.

The new solution reproduces all data for this reaction quite well, with the exception of the first two energy bins for Σ, where GRAAL data show a clear $\sim \sin\theta$ structure, see fig. 23. CLAS data are presently too uncertain to confirm or disprove this behavior. The models do not show any flexibility in that energy bin to possibly describe such a sine structure. This will be further discussed in sect. 5.

For $\gamma\, n \to \eta'\, n$ only one data set exists, the unpolarized cross sections measured by the CBELSA/TAPS Collaboration [72]. The data together with our full solution are presented in fig. 24. There is some disagreement in the range $W = 2077$–2121 MeV. This channel has not been analyzed by other PWA groups.

5 Narrow resonances in η and η' photoproduction

Around 2005, in η photoproduction on the neutron a bump in the total cross section in the vicinity of $W = 1685$ MeV was observed that was especially pronounced in the cross section ratio σ_n/σ_p [76–78]. Many attempts were made to explain this effect, some explanations introduced a new narrow $N(1685)$ resonance, where, however,

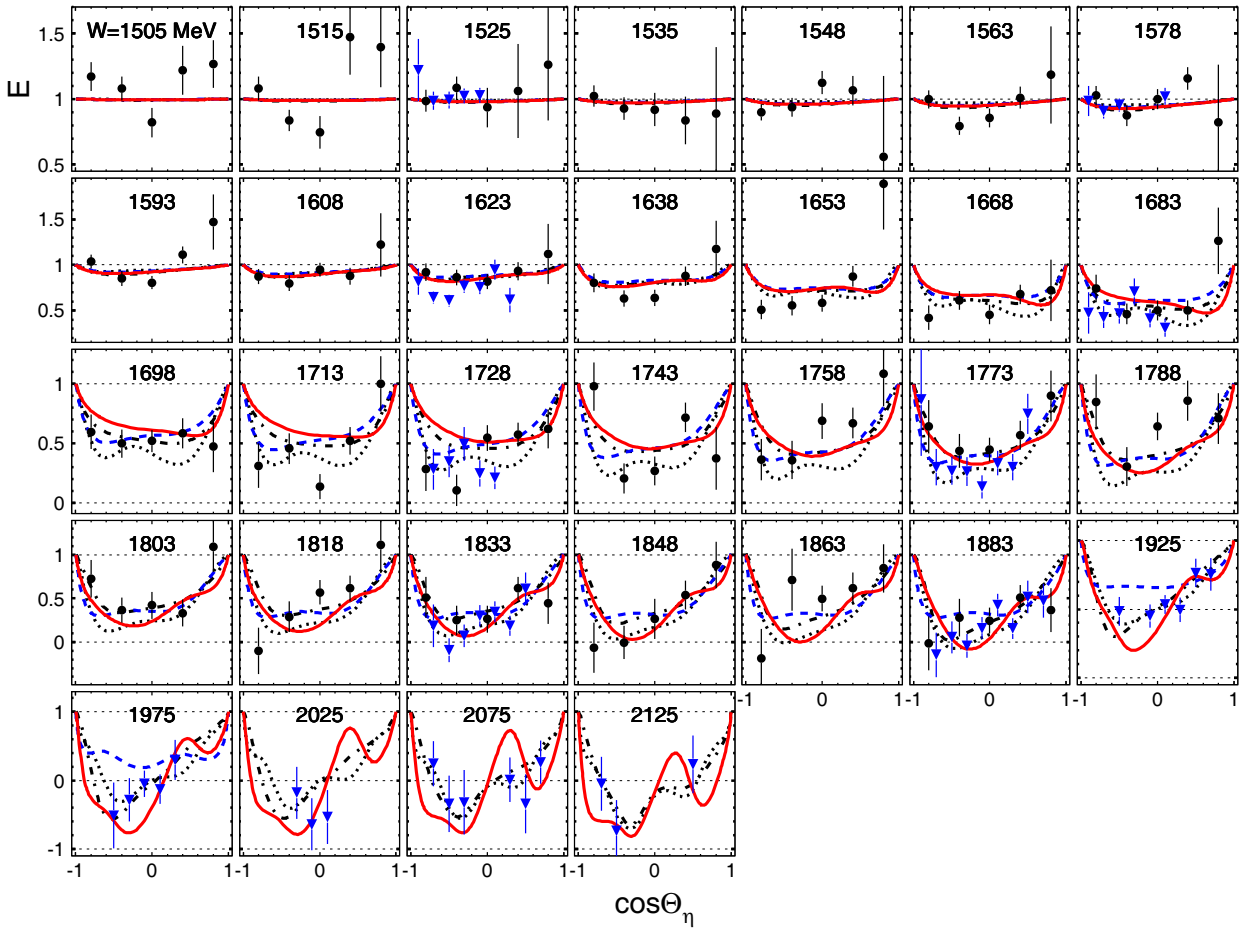

Fig. 16. Beam-target polarization asymmetry E for (γ,η) on the proton. The black circles and blue triangles are data from MAMI [65,66] and CLAS [64] respectively. Notation of the curves is as in fig. 14.

the quantum numbers were not uniquely determined [79, 80]. Mostly a P_{11} resonance was assumed, which also matched the position of a predicted non-strange pentaquark state [81]. The range of the width was determined as 15–45 MeV. Due to further lack of evidence and more conventional explanations of the bump structure in terms of interferences of S_{11} resonances, in 2016 PDG has decided to remove this state from the listings. For further reading see ref. [2].

Here we want to discuss a further attempt to study possible consequences from a narrow $N(1900)$ state, a few MeV above η' threshold. Anisovich *et al.* [82] have shown that a narrow $N(1900)\frac{3}{2}^-$ D_{13} resonance with a mass $M_R = 1900 \pm 1$ MeV and a total width of less than 3 MeV can explain the unexpected energy and angular dependence of the differential cross section $\mathrm{d}\sigma/\mathrm{d}\Omega$ from A2MAMI and of the beam asymmetry Σ from GRAAL. In our EtaMAID analysis we can confirm the possibility for an explanation with a narrow resonance, however, in EtaMAID we would obtain a narrow S_{11} resonance with quantum numbers $\frac{1}{2}^-$, mass $M_R = 1902.6 \pm 1.0$ MeV and width $\Gamma_R = 2.1 \pm 0.5$ MeV.

As it was pointed out before, the photon beam asymmetry Σ measured at GRAAL exhibits a very unexpected behavior. First of all, it shows a nodal structure with a sinus-type shape in the angular distribution, which is a sign of higher partial wave content compared to the beam asymmetry in threshold η photoproduction. Second, it appears with a strong energy behavior, changing the magnitude of the beam asymmetry significantly within only a few MeV. And third, it appears very close to the η' threshold and decreases strongly within only a few MeV. Naturally, in this region an effect would increase in magnitude rather than decrease, when the energy rises.

The first issue can be easily investigated by the partial wave series of the beam asymmetry. Expanded into partial waves up to F waves ($L_{max} = 3$), the beam asymmetry observable $\check{\Sigma}$ (see appendix C) can be expressed in its angular dependence up to x^4 with $x = \cos\theta$

$$\check{\Sigma} = \sigma_0(x)\Sigma(x) = (1 - x^2)\sum_{k=0}^{4} a_k\, x^k, \qquad (49)$$

where the observed nodal structure arises from the coefficient a_1, which can be separated into S-F, P-D and D-F interferences of partial waves, $a_1 = a_1^{SF} + a_1^{PD} + a_1^{DF}$. Using eq. (A.2) and the partial wave expansion of the CGLN

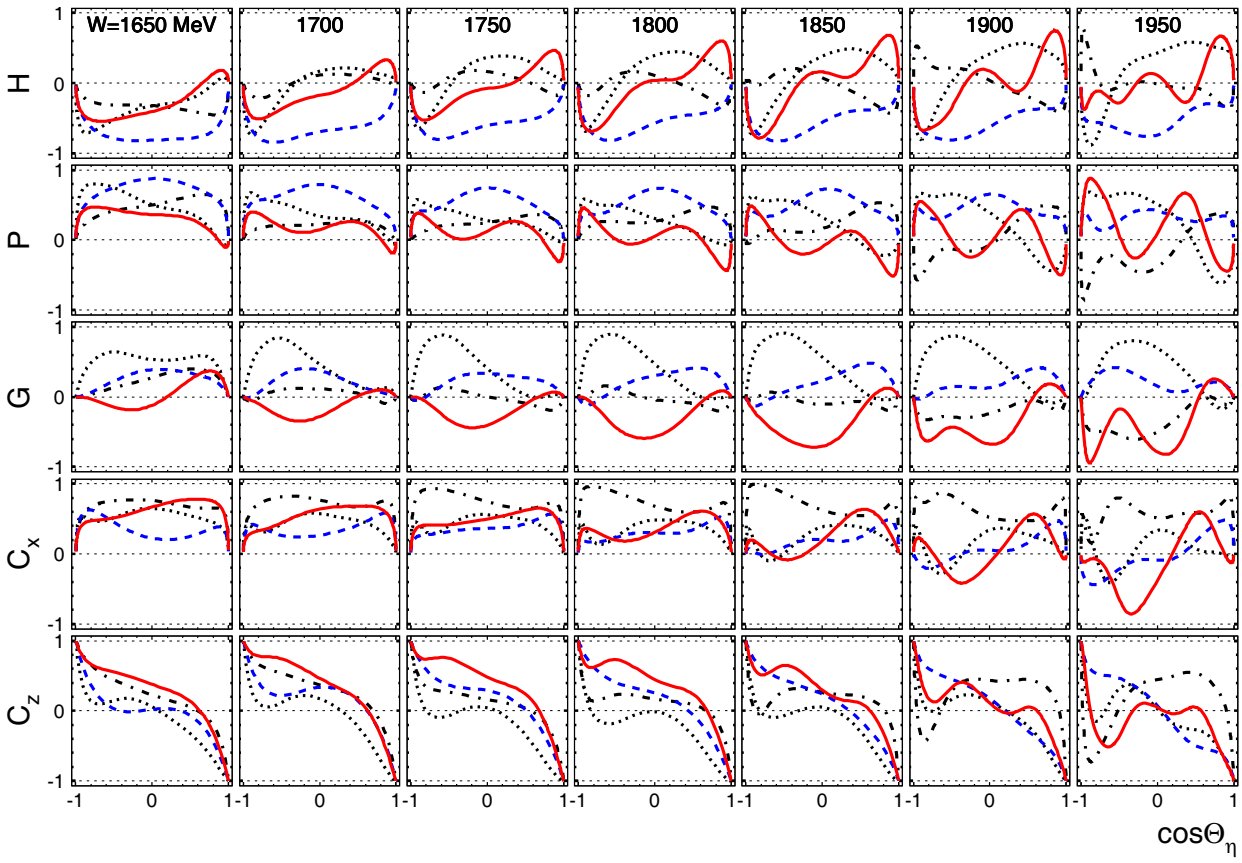

Fig. 17. Predictions for P, H, G, C_x, and C_z observables for (γ,η) on the proton. Notations of the curves are as in fig. 14.

amplitudes, we get in details

$$
\begin{aligned}
a_1^{S_{11}-F_{15}} &= 15\,\mathrm{Re}\{E_{0+}^*(E_{3-}+M_{3-})\},\\
a_1^{S_{11}-F_{17}} &= 15\,\mathrm{Re}\{E_{0+}^*(E_{3+}-M_{3+})\},\\
a_1^{P_{11}-D_{15}} &= 15\,\mathrm{Re}\{M_{1-}^*(M_{2+}-E_{2+})\},\\
a_1^{P_{13}-D_{13}} &= 18\,\mathrm{Re}\{E_{1+}^*E_{2-}+M_{1+}^*M_{2-}\},\\
a_1^{P_{13}-D_{15}} &= 3\,\mathrm{Re}\{-9E_{1+}^*E_{2+}+M_{1+}^*(5E_{2+}+4M_{2+})\},\\
a_1^{D_{13}-F_{15}} &= -3\,\mathrm{Re}\{E_{2-}^*(4E_{3-}-5M_{3-})-9M_{2-}^*M_{3-}\},\\
a_1^{D_{13}-F_{17}} &= -15\,\mathrm{Re}\{E_{2-}^*(5E_{3+}+M_{3+})+6M_{2-}^*M_{3+}\},\\
a_1^{D_{15}-F_{15}} &= -\frac{189}{2}\,\mathrm{Re}\{E_{2+}^*E_{3-}+M_{2+}^*M_{3-}\}. \qquad (50)
\end{aligned}
$$

Interferences of P_{11}-D_{13} and D_{15}-F_{17} do not contribute.

In fig. 25 we show our result with a narrow $S_{11}(1900)$ and the BnGa solution with a narrow $D_{13}(1900)$ for η' photoproduction on the proton. Both solutions can describe the GRAAL data similarly well, whereas without a narrow resonance both solutions predict an almost zero value for the threshold beam asymmetry, see fig. 23. According to the multipole expansion of the a_1 coefficient, eq. (50), the nodal structure of the angular dependence of the beam asymmetry is explained with a S_{11}-F_{15} interference in EtaMAID and with a P_{13}-D_{13} interference in BnGa.

Besides the beam asymmetry, also the differential cross section exhibits small unexplained structures in the standard solutions, see fig. 22. This is also much improved with the inclusion of a narrow resonance as shown in fig. 26.

With the two energy bins of the GRAAL beam asymmetry and the lowest energy bins of the A2MAMI differential cross sections, the evidence for the existence of a narrow resonance is rather weak. Especially, as with only two observables the quantum numbers of such a state cannot uniquely be determined. Therefore, we investigate the effects of such narrow resonances on further not yet measured polarization observables using beam and target polarization. In fig. 27 we show the standard solutions and the addition of narrow resonances from EtaMAID and BnGa on the full set of 8 polarization observables that could be measured with beam- and target-polarization techniques, without recoil polarization detection.

For such narrow resonances small energy bins are certainly needed. The differential cross section, which can be expected with highest statistics, should be re-measured and analyzed in finer energy bins. Most important, due to the nodal structure change, is a new measurement of the photon beam asymmetry, aiming for a similar precision as in the GRAAL measurement. P and H observables, which are almost identical up to a sign, are sensitive to a narrow D_{13} resonance, but almost independent of a narrow S_{11} state. Also T and F observables are less sensitive but could be obtained at MAMI with high accuracy.

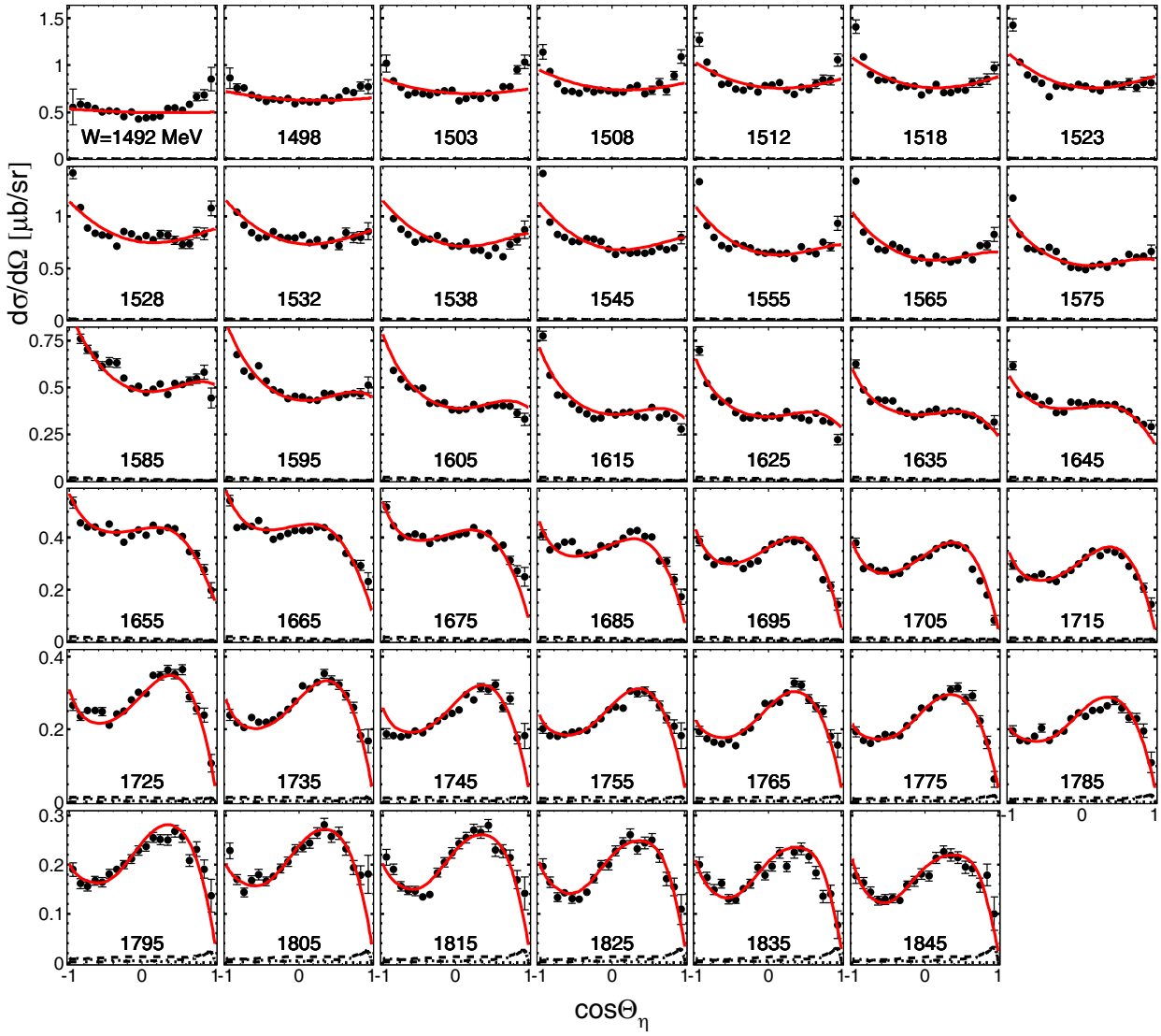

Fig. 18. Differential cross section for (γ, η) on the neutron. The red solid lines show our full solutions, whereas the black dotted, dash-dotted and dashed lines are Born terms, Regge, and full background, respectively. The data are from A2MAMI [67].

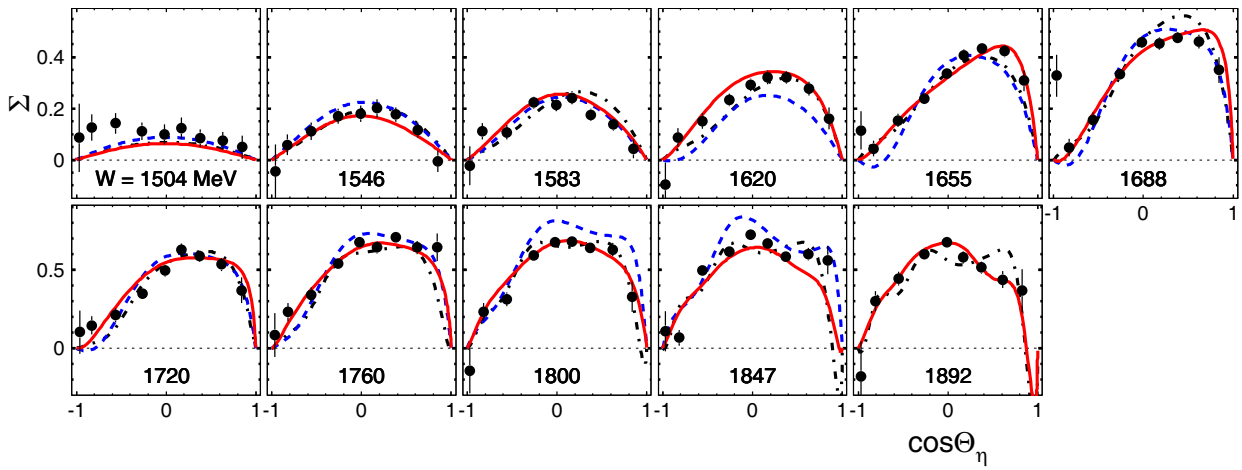

Fig. 19. Photon beam asymmetry Σ for (γ, η) on the neutron. The data are from GRAAL [70]. The solid red lines show our full solution. Results of other PWA analyses are shown by the black dotted (BnGa [34]), and blue dashed (KSU [37]) lines.

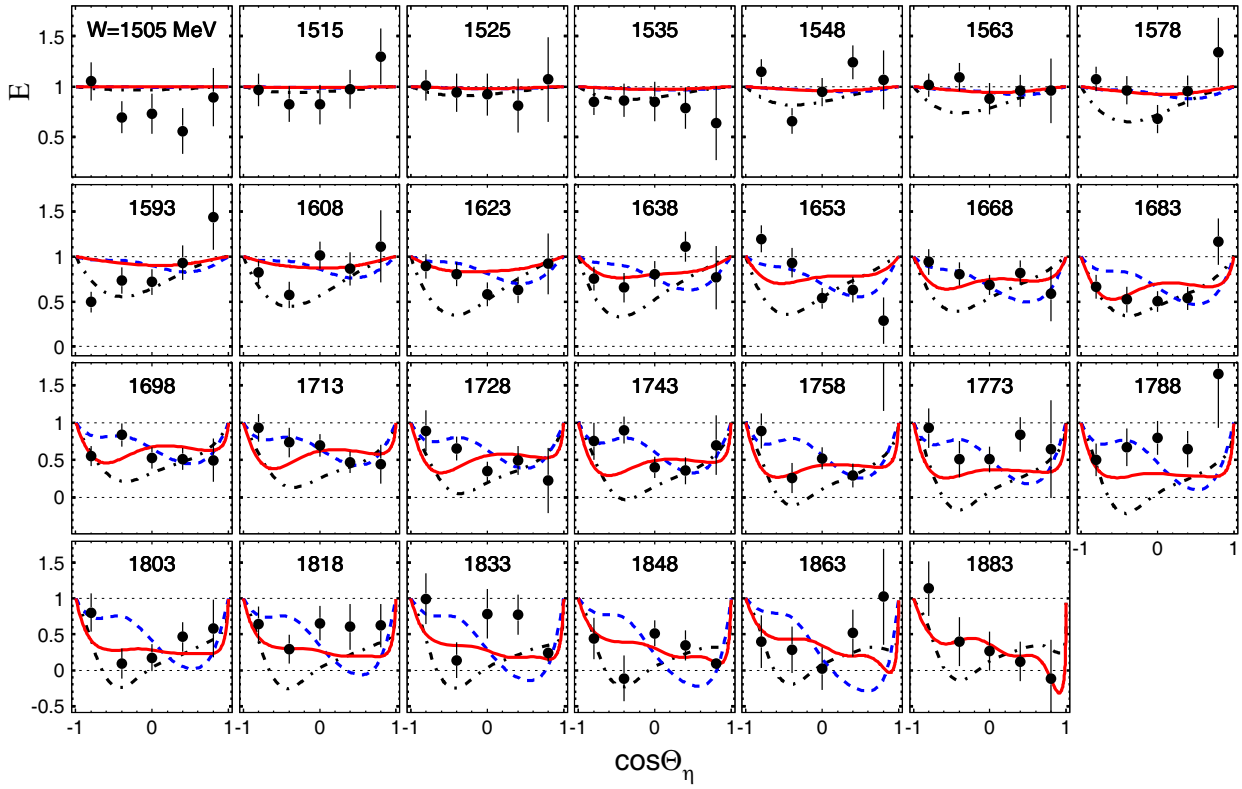

Fig. 20. Beam-target polarization asymmetry E for (γ, η) on the neutron. The data are from A2MAMI [65, 66]. Notation of the curves is as in fig. 19.

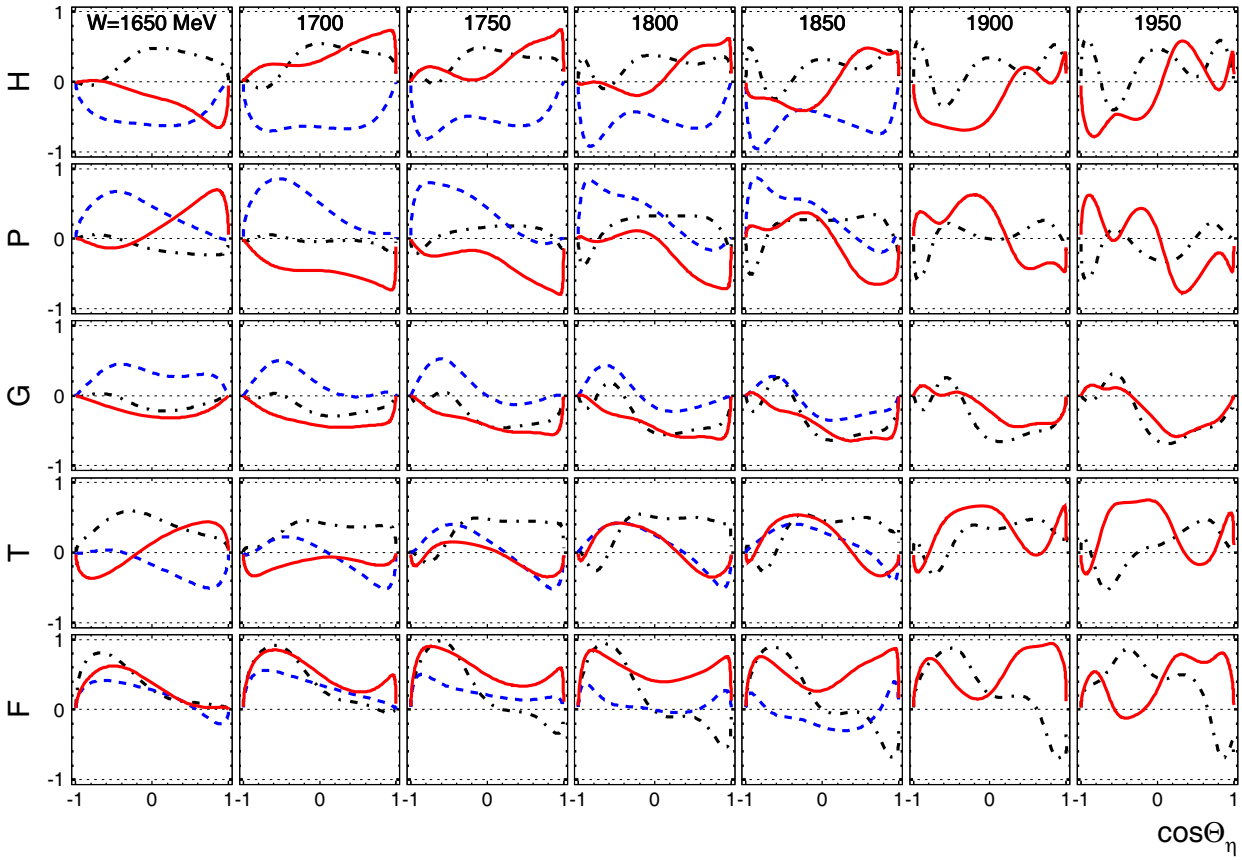

Fig. 21. Predictions for P, H, G, T and F observables for (γ, η) on the neutron. Notation of the curves is as in fig. 19.

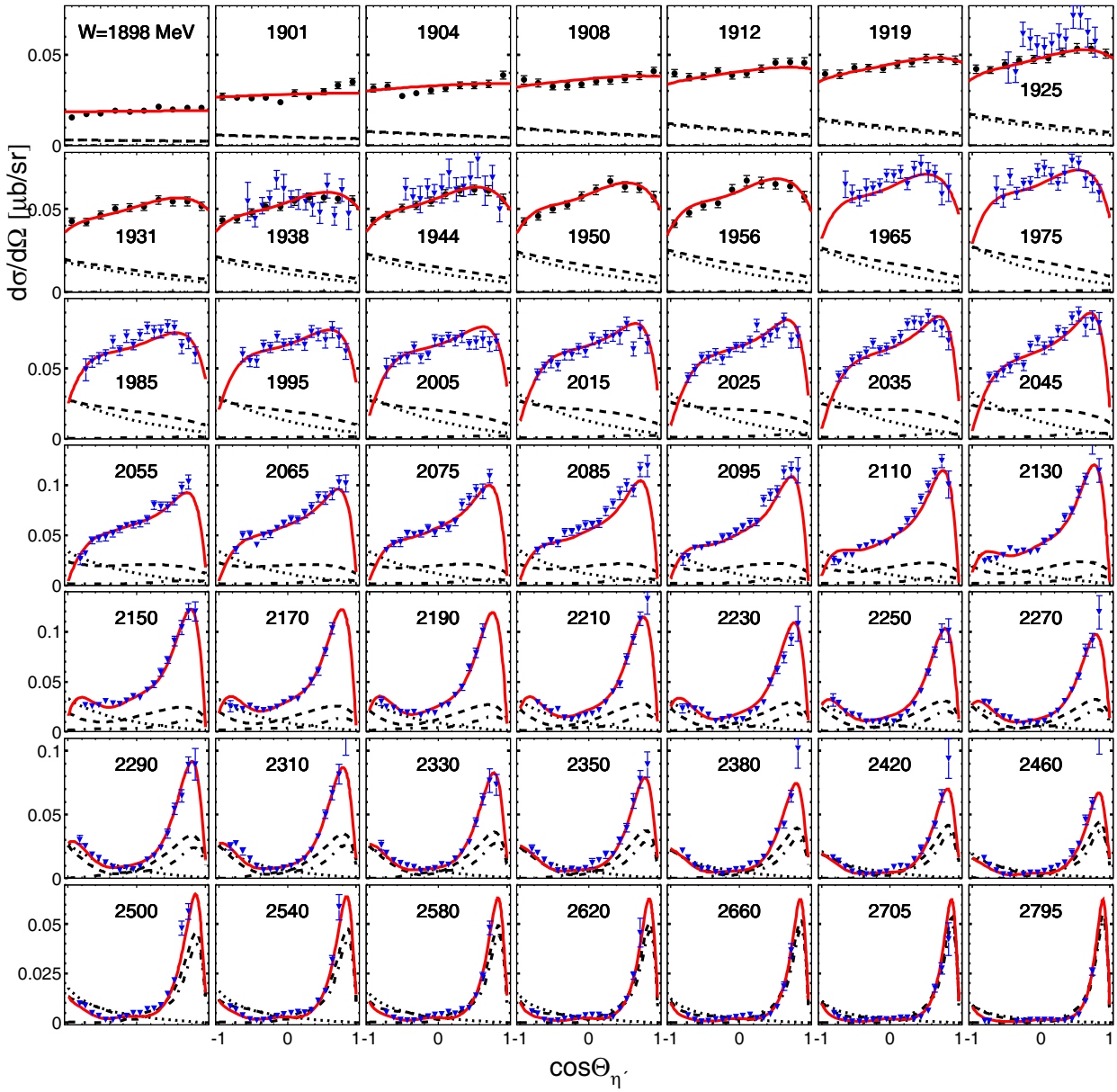

Fig. 22. Differential cross section for (γ, η') on the proton. The red solid lines show our full solutions, whereas the black dotted, dash-dotted, and dashed lines are Born terms, Regge, and full background, respectively. The black circles are data from A2MAMI [58] and blue triangles from CLAS [59].

6 Partial wave amplitudes

Compared to pion photoproduction, a comparison of partial waves from different PWA is not straightforward in η or η' photoproduction. First of all, different conventions for isospin matrix elements are used in the literature, which appear as $+1$ in the BnGa, JüBo and KSU analysis and -1 in the MAID and SAID analysis. This overall sign or phase convention is denoted as $C_{\eta N}$ in our BW ansatz of eq. (34). Second, for η and η' photoproduction no such convenient unitarity constraints as the Watson Theorem exist, that determine the phases in the low-energy regime. The only, somewhat weaker constraints arise from channel couplings, which is more advanced in coupled-channels approaches as BnGa, JüBo and KSU. In EtaMAID we introduce coupling to pion channels only via the Breit-Wigner ansatz and the parametrization of the energy dependent widths. *E.g.*, the $N(1535)\frac{1}{2}^-$ provides a very strong constraint because of its large branchings of about 50% for πN and 40% for ηN. For other partial waves, such BW constraints are much less effective.

Therefore, even if complete experiments were performed, final ambiguities would remain, which could not be resolved by experimental observables. All physical observables are sums of bi-linear products of amplitudes and conjugated amplitudes, *e.g.* $\mathrm{Re}\{H_i(W,\theta)\, H_j^*(W,\theta)\}$, and are therefore invariant under an overall energy- and angle-dependent phase $\phi(W,\theta)$. This phase depends very much

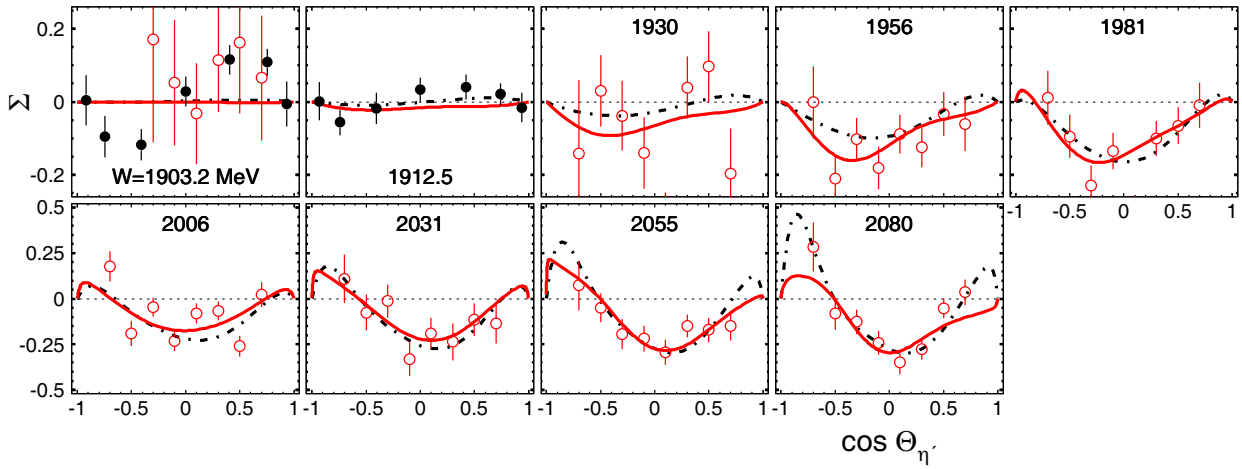

Fig. 23. Photon beam asymmetry Σ for (γ, η') on the proton. The black full and red opened circles are data from GRAAL [71] and CLAS [62], respectively. Notation of the curves as in fig. 14.

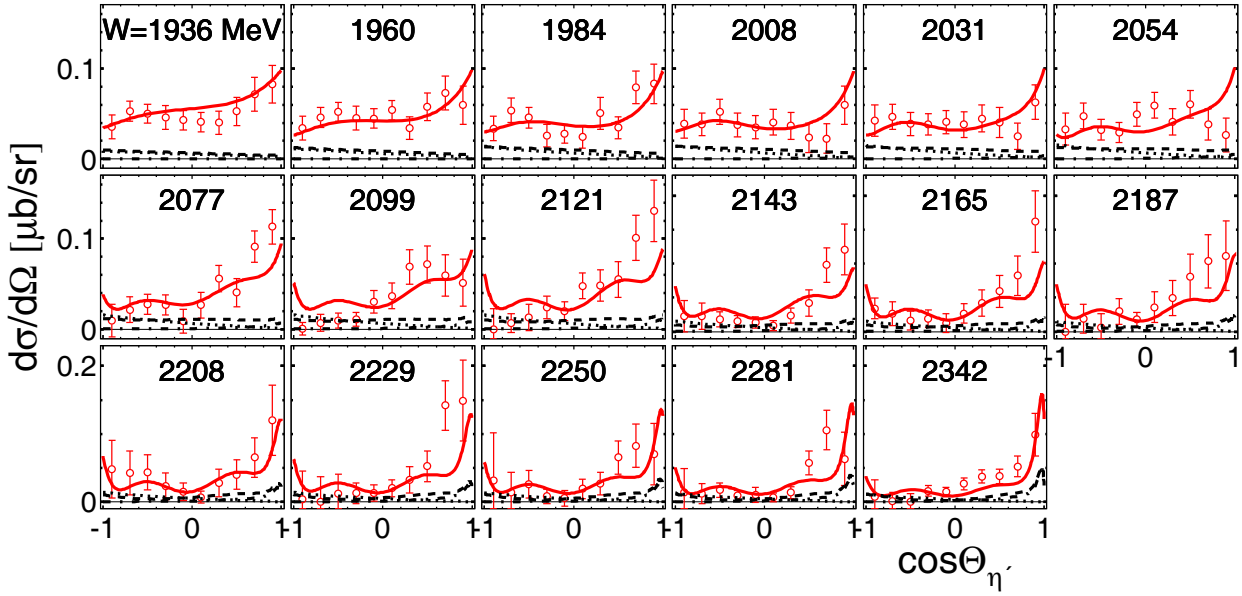

Fig. 24. Differential cross section for (γ, η') on the neutron. The solid red lines show our full solutions, whereas the black dotted, dash-dotted, and dashed lines are Born terms, Regge, and full background, respectively. The data points are from CBELSA/TAPS [72].

on the models and on couplings with other channels, which finally will always be incomplete.

For a better comparison between the different newly updated 2018 PWA, that all use practically the same database, we have performed a phase rotation of all amplitudes to our EtaMAID2018 phase,

$$H_i^{BG} \rightarrow \tilde{H}_i^{BG} = H_i^{BG} \cdot e^{i(\phi_{H1}^{MD}(W,\theta) - \phi_{H1}^{BG}(W,\theta))}, \quad i = 1, \ldots, 4, \tag{51}$$

where MD stands for the EtaMAID model and BG for any other PWA, as BnGa, JüBo, and KSU. For a detailed discussion of angle-dependent phase ambiguities, see refs. [83, 84].

In figs. 28 and 29 we compare the multipoles from rotated helicity amplitudes of EtaMAID, BnGa, JüBo, and KSU. While the S wave is practically identical among all solutions, all other partial waves show deviations from small up to huge. Moderate deviations we can see in E_{1+}, M_{1+}, E_{2-}, and M_{3-}, those we can already expect from different fits to the measured data, as can be seen in sect. 4. Other partial waves as M_{1-} and especially E_{2+} show very large deviations, which are most likely due to the incompleteness of the database, where such ambiguities must be expected.

A possible solution of this problem could be obtained along the lines of ref. [39] by using constraints from fixed-t

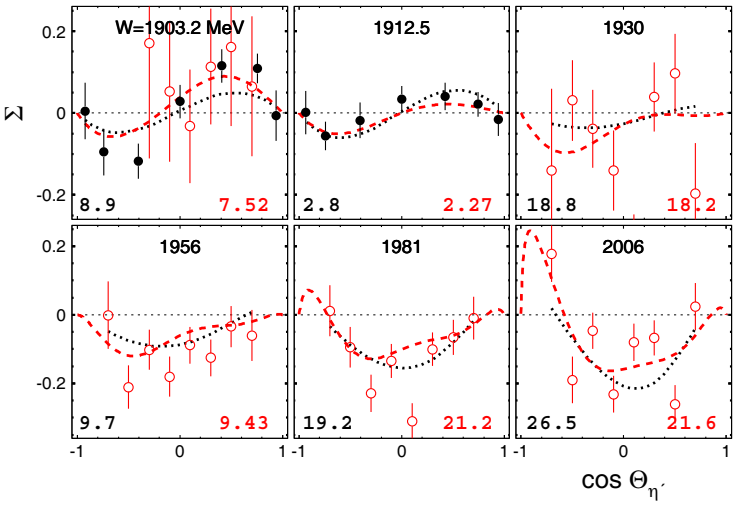

Fig. 25. Photon beam asymmetry Σ for (γ, η') on the proton for selected energy bins. The black full and red open circles are data from GRAAL [71] and CLAS [62], respectively. The dashed red lines show our solution with a narrow $S_{11}(1900)$ resonance and corresponding χ^2 in the lower right corner for each panel and the black dotted lines BnGa [82] with a narrow $D_{13}(1900)$ resonance and χ^2 on the left.

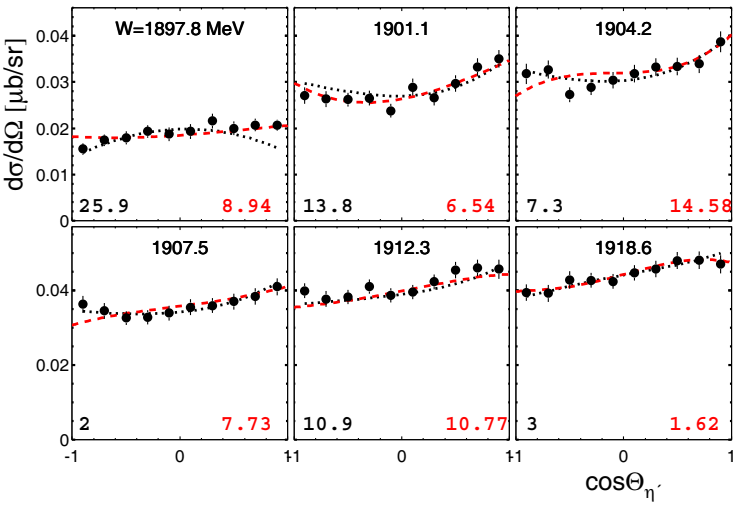

Fig. 26. Differential cross section for (γ, η') on the proton for selected energy bins. The black circles are data from A2MAMI [58]. Notations are as in fig. 25.

analyticity. But in addition also improvements of the database with further observables and higher statistics would be very helpful.

7 Summary and conclusions

Here we present a new update of EtaMAID for η and η' photoproduction with four channels, ηp, ηn, $\eta' p$, $\eta' n$. A large amount of data has been measured during the last decade, mostly from A2MAMI, CBELSA and CLAS. Some of the new polarization observables showed large discrepancies with our previous solutions EtaMAID2001 and EtaMAID2003, and gave therefore a lot of insight in further details of the partial wave analysis. In a new approach, the high-energy regime $W > 2.5$ GeV was first described with a Regge approach, and the resonance regime from threshold up to $W < 2.5$ GeV with 21 N^* resonances for (γ, η) and 12 N^* resonances for (γ, η'). All known N^* states listed by PDG have been investigated and, except for only 2 cases, an improvement in our fit was found. Resonances found to be insignificant for our analysis are $N(2040)\frac{3}{2}^+$ (a one-star state only seen in J/Ψ decays) and $N(2220)\frac{9}{2}^+$ (a four-star high spin state mainly seen in πN). In order to avoid or at least strongly reduce the double counting from Regge plus resonances, we introduced damping factors for Born and t-channel exchange contributions.

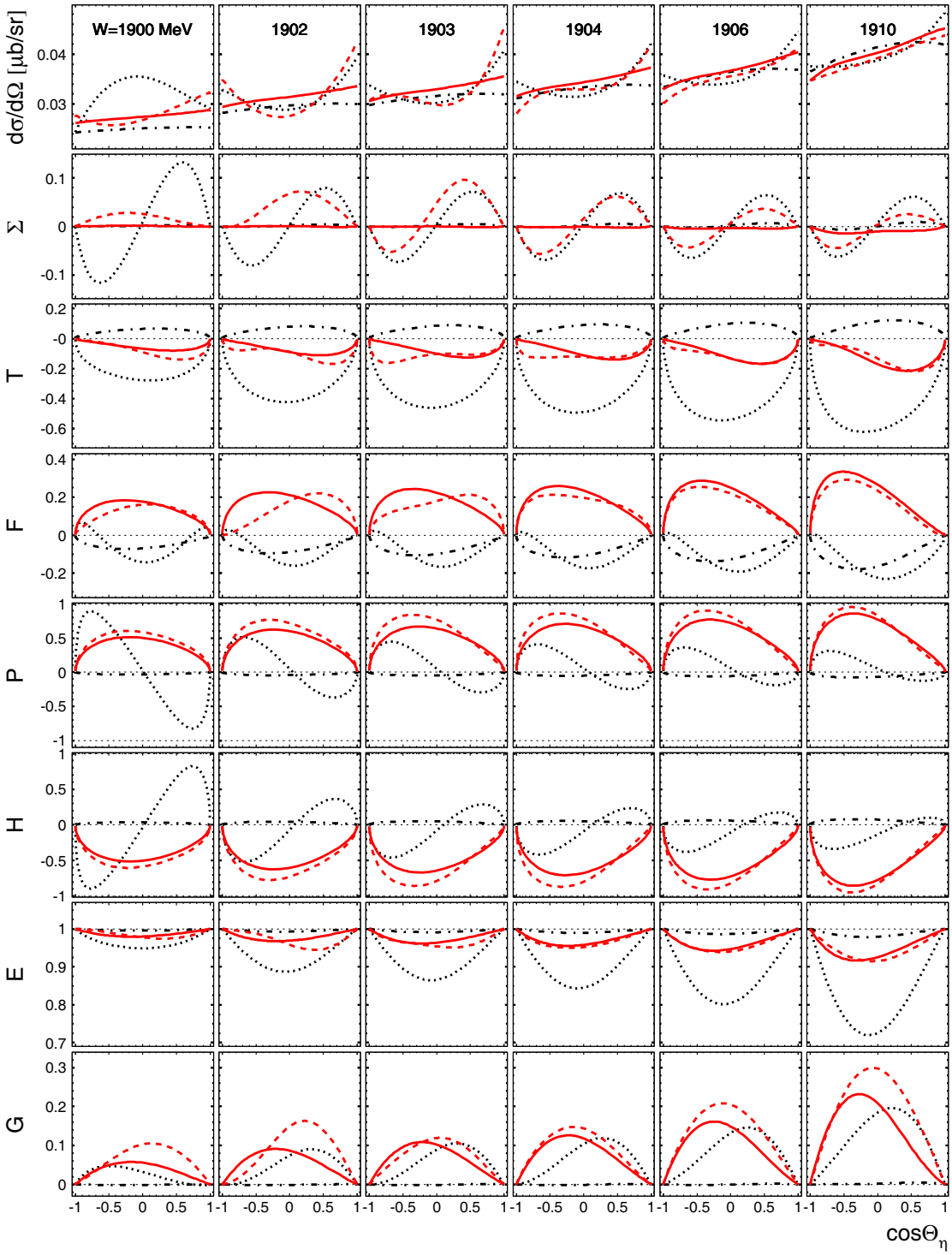

Fig. 27. Predictions for all 8 single- and beam-target double polarization observables for (γ, η') on the proton. The red solid and black dash-dotted lines are the 2018 standard solutions of EtaMAID and BnGa without narrow resonances. The red dashed lines show the predictions of our EtaMAID solution with a narrow $S_{11}(1900)$ resonance, while the black dotted lines are obtained with the BnGa solution and a narrow $D_{13}(1900)$ resonance [82].

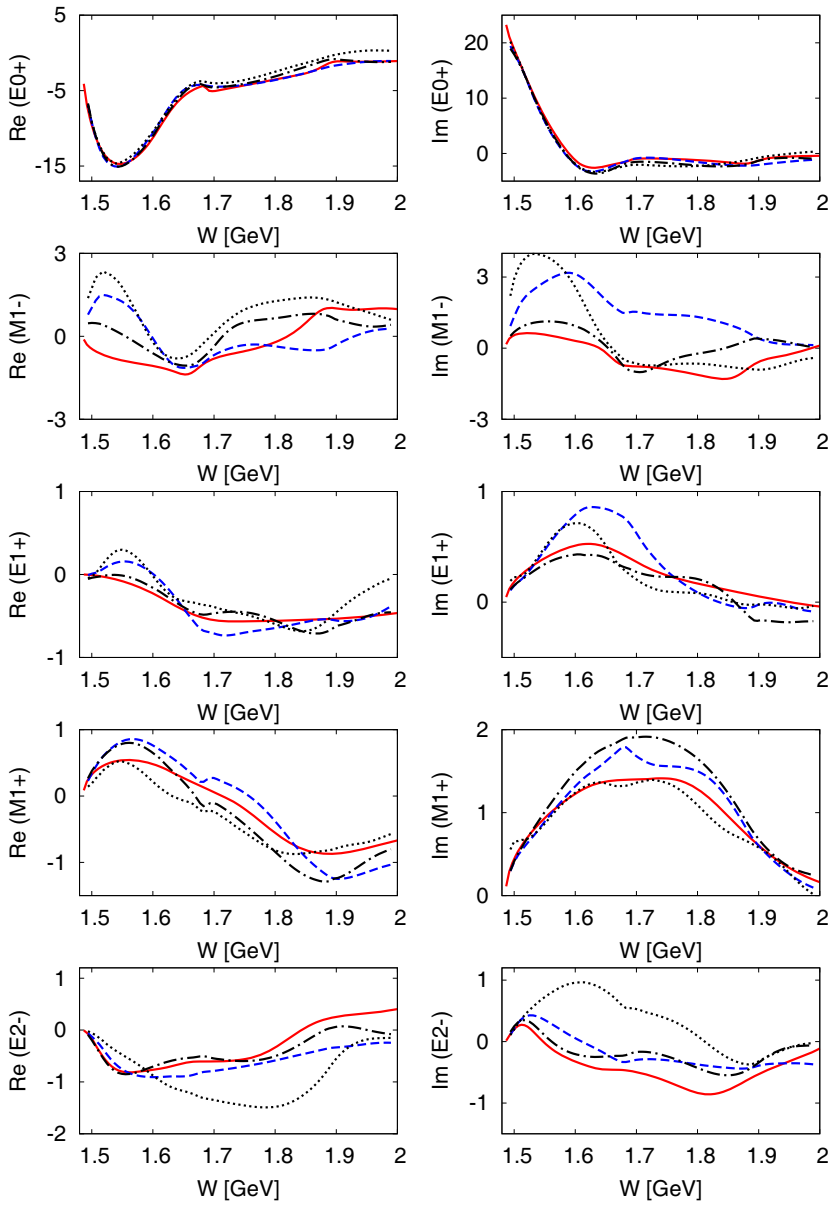

Fig. 28. Comparison of $E_{0+}(S_{11})$, $M_{1-}(P_{11})$, $E_{1+}(P_{13})$, $M_{1+}(P_{13})$, and $E_{2-}(D_{13})$ multipoles for $\gamma p \to \eta p$, obtained from rotated helicity amplitudes (see eq. (51)) of different PWA. The solid red lines show our EtaMAID2018 solution. Results of other PWA analyses are shown by the black dash-dotted (BnGa [35]), the black dotted (JüBo [36]), and the blue dashed (KSU [37]) lines. The multipoles are given in units of mfm.

We obtained very good fits to almost all data, except for some cases, where data from MAMI and CBELSA were in conflict and it did not make sense to use both in the database for our fit. In these cases we decided to use the MAMI data. From all N^* resonances that were significantly improving our fits, we found the largest contributions in (γ,η) from: $N(1535)\frac{1}{2}^-$, $N(1650)\frac{1}{2}^-$, $N(1895)\frac{1}{2}^-$, $N(1710)\frac{1}{2}^+$, $N(1720)\frac{3}{2}^+$, $N(1900)\frac{3}{2}^+$, $N(1520)\frac{3}{2}^-$, $N(1700)\frac{3}{2}^-$, and $N(1875)\frac{3}{2}^-$. For (γ,η') these are $N(1895)\frac{1}{2}^-$, $N(1880)\frac{1}{2}^+$, $N(2100)\frac{1}{2}^+$, $N(2000)\frac{5}{2}^+$, and $N(1990)\frac{7}{2}^+$. While $N(1700)\frac{3}{2}^-$ and $N(1710)\frac{1}{2}^+$ are practically neutron resonances, $N(1650)\frac{1}{2}^-$ and $N(1880)\frac{1}{2}^+$ are much larger in the proton channel. Other resonances contribute about equally in the proton and neutron channels, see also photon couplings in table 6 of appendix C.

Generally, in a Breit-Wigner resonance analysis, the resonance parameters are subject to model dependence. This could be rather weak for prominent resonances with widths $\Gamma \lesssim 120\,\text{MeV}$, but for broad resonances with

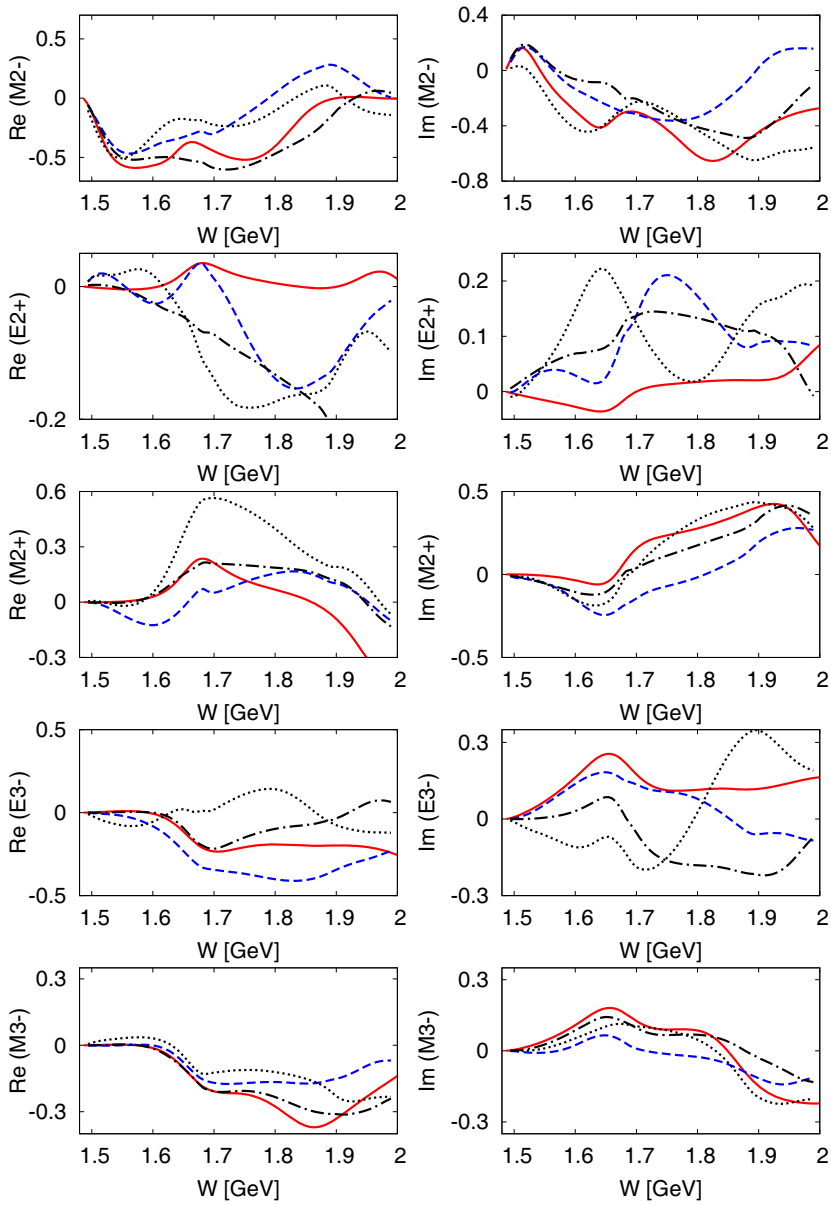

Fig. 29. Comparison of $M_{2-}(D_{13})$, $E_{2+}(D_{15})$, $M_{2+}(D_{15})$, $E_{3-}(F_{15})$, and $M_{3-}(F_{15})$ multipoles from different PWA. Further details as in fig. 28.

widths of several hundred MeV, the model dependence can be very large. In an upcoming work we plan to perform a detailed resonance analysis with a search of t-matrix poles and residues. In an application of the L+P method, successfully applied in pion elastic scattering and pion photoproduction, we can expect to reduce the model dependence for the resonance properties considerably.

The new solution EtaMAID2018 is online available on the MAID web pages [4].

We want to thank Deborah Rönchen of the Jülich-Bonn, Victor Nikonov of the Bonn-Gatchina, and Mark Manley of the Kent State University Collaborations for providing us with their most recent partial wave results and Andrey Sarantsev for many helpful discussions. This work was supported by the Deutsche Forschungsgemeinschaft (SFB 1044).

Appendix A. Observables expressed in CGLN amplitudes

Here we give the differential cross section, the three single-spin asymmetries and the eight beam-target and beam-recoil double-polarization observables expressed in CGLN amplitudes. In addition we give the combination $\check{P} + \check{H}$, where most of the terms cancel. A full list of all polar-

Table 5. Hadronic Breit-Wigner parameters for nucleon resonances. Masses M_R and widths Γ_R are given in MeV and the branching ratios β in %. The coupling constants g are dimensionless. The damping parameters of the hadronic vertex functions are fixed at $X = 450\,\mathrm{MeV}$. For channel openings below threshold, conventional branching ratios are not defined and are marked with $-$. Further non-zero couplings are also found for $N(1440)\frac{1}{2}^+$ with $g_{\eta N} = 1.0$, for $N(1650)\frac{1}{2}^-$ with $g_{K\Sigma} = 1.21$ and for $N(1710)\frac{1}{2}^+$ with $g_{\omega N} = 0.907$.

$N(\cdots)J^\pi$	ℓ	$\zeta_{\eta N}$	$\zeta_{\eta' N}$	M_R	Γ_R	$\beta_{\pi N}$	$\beta_{\pi\pi N}$	$\beta_{\eta N}$	$\beta_{K\Lambda}$	$\beta_{K\Sigma}$	$\beta_{\omega N}$	$\beta_{\eta' N}$	$g_{\eta' N}$
$N(1440)\frac{1}{2}^+$	1	+1		1430.0	350.0	65.0	35.0	–	–	–	–	–	0
$N(1520)\frac{3}{2}^-$	2	+1		1520.0	100.0	61.0	38.9	0.08	–	–	–	–	0
$N(1535)\frac{1}{2}^-$	0	+1		1521.7	174.7	52.0	13.6	34.4	–	–	–	–	0
$N(1650)\frac{1}{2}^-$	0	−1		1626.3	132.5	51.0	27.2	18.8	3.0	–	–	–	0
$N(1675)\frac{5}{2}^-$	2	−1		1680.0	100.0	41.0	57.1	0.93	1.0	–	–	–	0
$N(1680)\frac{5}{2}^+$	3	+1		1690.0	145.3	62.0	37.8	0.15	0	–	–	–	0
$N(1700)\frac{3}{2}^-$	2	+1		1659.6	83.9	15.0	80.8	1.15	3.0	0	–	–	0
$N(1710)\frac{1}{2}^+$	1	+1		1669.5	63.2	5.0	68.2	11.8	15.0	0	–	–	0
$N(1720)\frac{3}{2}^+$	1	+1		1750.0	395.5	11.0	79.7	1.28	8.0	0	–	–	0
$N(1860)\frac{5}{2}^+$	3	−1	+1	1885.8	197.4	20.0	76.5	3.54	0	0	0	–	0.700
$N(1875)\frac{3}{2}^-$	2	+1	−1	1893.9	320.0	4.0	46.0	11.0	4.0	15.0	20.0	–	0.168
$N(1880)\frac{1}{2}^+$	1	+1	−1	1882.1	90.0	6.0	74.6	0.43	2.0	17.0	0	–	0.400
$N(1895)\frac{1}{2}^-$	0	+1	+1	1894.4	70.7	2.5	63.2	3.27	18.0	13.0	0	–	0.405
$N(1900)\frac{3}{2}^+$	1	−1	−1	1898.7	450.0	3.0	63.9	3.06	12.0	5.0	13.0	0.03	0.563
$N(1990)\frac{7}{2}^+$	3	+1	+1	2227.0	389.0	2.0	89.9	3.60	0	0	0	4.5	0.347
$N(2000)\frac{5}{2}^+$	3	−1	+1	2116.8	246.9	8.0	87.3	2.30	0	0	0	2.4	0.300
$N(2060)\frac{5}{2}^-$	2	+1	−1	1984.5	159.8	11.0	84.1	1.58	0	3.0	0	0.3	0.130
$N(2100)\frac{1}{2}^+$	1	+1	+1	2010.0	260.0	16.0	78.2	1.69	0	0	0	4.1	0.300
$N(2120)\frac{3}{2}^-$	2	+1	−1	2061.3	101.9	5.0	94.9	0.05	0	0	0	0.03	0.021
$N(2190)\frac{7}{2}^-$	4	−1	+1	2250.0	591.2	16.0	78.8	4.53	0.5	0	0	0.18	0.100
$N(2250)\frac{9}{2}^-$	4	+1	−1	2250.0	733.2	12.0	84.4	3.49	0	0	0	0.10	0.085

ization observables including also target-recoil polarization expressed in CGLN and in helicity amplitudes can be found in ref. [39]. In the literature, the sign definitions of double-polarization observables is not unique. For an overview of the conventions see ref. [85]. Here we follow the conventions by Barker [38], SAID [86] and MAID [5].

$$\sigma_0 = \mathrm{Re}\{F_1^* F_1 + F_2^* F_2 + \sin^2\theta\,(F_3^* F_3/2 + F_4^* F_4/2 + F_2^* F_3 + F_1^* F_4 + \cos\theta\, F_3^* F_4) - 2\cos\theta\, F_1^* F_2\}\rho \tag{A.1}$$

$$\check{\Sigma} = -\sin^2\theta\,\mathrm{Re}\,\{(F_3^* F_3 + F_4^* F_4)/2 + F_2^* F_3 + F_1^* F_4 + \cos\theta\, F_3^* F_4\}\,\rho \tag{A.2}$$

$$\check{T} = \sin\theta\,\mathrm{Im}\,\{F_1^* F_3 - F_2^* F_4 + \cos\theta\,(F_1^* F_4 - F_2^* F_3) - \sin^2\theta\, F_3^* F_4\}\,\rho \tag{A.3}$$

$$\check{P} = -\sin\theta\,\mathrm{Im}\,\{2F_1^* F_2 + F_1^* F_3 - F_2^* F_4 + \cos\theta\,(F_1^* F_4 - F_2^* F_3) - \sin^2\theta\, F_3^* F_4\}\,\rho \tag{A.4}$$

$$\check{E} = \mathrm{Re}\,\{F_1^* F_1 + F_2^* F_2 - 2\cos\theta\, F_1^* F_2 + \sin^2\theta\,(F_2^* F_3 + F_1^* F_4)\}\,\rho \tag{A.5}$$

$$\check{F} = \sin\theta\,\mathrm{Re}\,\{F_1^* F_3 - F_2^* F_4 - \cos\theta\,(F_2^* F_3 - F_1^* F_4)\}\,\rho \tag{A.6}$$

$$\check{G} = \sin^2\theta\,\mathrm{Im}\,\{F_2^* F_3 + F_1^* F_4\}\,\rho \tag{A.7}$$

$$\check{H} = \sin\theta\,\mathrm{Im}\,\{2F_1^* F_2 + F_1^* F_3 - F_2^* F_4 + \cos\theta\,(F_1^* F_4 - F_2^* F_3)\}\,\rho \tag{A.8}$$

$$\check{P} + \check{H} = \sin^3\theta\,\mathrm{Im}\,\{F_3^* F_4\}\,\rho \tag{A.9}$$

$$\check{C}_{x'} = \sin\theta\,\mathrm{Re}\,\{F_1^* F_1 - F_2^* F_2 - F_2^* F_3 + F_1^* F_4 - \cos\theta\,(F_2^* F_4 - F_1^* F_3)\}\,\rho \tag{A.10}$$

$$\check{C}_{z'} = \mathrm{Re}\,\{2F_1^* F_2 - \cos\theta\,(F_1^* F_1 + F_2^* F_2) + \sin^2\theta\,(F_1^* F_3 + F_2^* F_4)\}\,\rho \tag{A.11}$$

Table 6. Electromagnetic Breit-Wigner parameters for nucleon resonances. Photon couplings ${}_NA_\lambda$ are given in $10^{-3}/\sqrt{\text{GeV}}$. Unitary phases ϕ are given in degrees. The damping parameters of the electromagnetic vertex functions are fixed at $X_\gamma = 0$.

$N(\cdots)J^\pi$	${}_pA_{1/2}$	${}_pA_{3/2}$	${}_nA_{1/2}$	${}_nA_{3/2}$	$\phi_{\eta p}$	$\phi_{\eta n}$	$\phi_{\eta' p}$	$\phi_{\eta' n}$
$N(1440)\frac{1}{2}^+$	−60.0	0	40.0	0	−0.4	−89.0	0	0
$N(1520)\frac{3}{2}^-$	−39.7	116.8	−160.0	−94.0	55.3	73.5	0	0
$N(1535)\frac{1}{2}^-$	115.0	0	−101.9	0	29.0	28.2	0	0
$N(1650)\frac{1}{2}^-$	55.0	0	−25.4	0	6.0	15.5	0	0
$N(1675)\frac{5}{2}^-$	23.7	20.0	−9.8	43.2	78.4	59.1	0	0
$N(1680)\frac{5}{2}^+$	−29.4	133.0	129.7	10.0	64.6	89.0	0	0
$N(1700)\frac{3}{2}^-$	15.2	−14.0	93.4	−32.1	60.9	57.7	0	0
$N(1710)\frac{1}{2}^+$	5.5	0	−42.2	0	−47.1	−79.4	0	0
$N(1720)\frac{3}{2}^+$	100.0	7.7	−64.9	63.9	87.8	56.3	0	0
$N(1860)\frac{5}{2}^+$	−30.7	29.0	−24.5	33.7	−83.0	−89.0	−39.6	−61.3
$N(1875)\frac{3}{2}^-$	18.0	−35.4	−32.0	50.4	34.6	30.3	−20.8	86.2
$N(1880)\frac{1}{2}^+$	60.4	0	−6.6	0	84.9	89.0	89.0	60.7
$N(1895)\frac{1}{2}^-$	−32.0	0	42.9	0	51.5	58.9	57.8	41.0
$N(1900)\frac{3}{2}^+$	−50.2	−67.0	−42.5	17.9	47.6	89.0	43.4	89.0
$N(1990)\frac{7}{2}^+$	−12.4	57.0	−43.3	−28.1	6.3	3.7	11.8	−7.9
$N(2000)\frac{5}{2}^+$	−73.1	−12.9	12.8	−59.2	89.0	51.5	89.0	50.8
$N(2060)\frac{5}{2}^-$	21.3	62.0	43.0	6.1	70.6	67.3	89.0	89.0
$N(2100)\frac{1}{2}^+$	63.9	0	−82.7	0	89.0	14.5	58.1	36.3
$N(2120)\frac{3}{2}^-$	113.5	160.0	160.0	100.0	−26.2	−89.0	56.6	24.3
$N(2190)\frac{7}{2}^-$	26.7	60.0	34.5	18.7	−89.0	−89.0	59.2	7.5
$N(2250)\frac{9}{2}^-$	−31.2	−20.0	24.1	12.5	82.8	89.0	89.0	88.2

$$\check{O}_{x'} = \sin\theta\,\mathrm{Im}\,\{F_2^* F_3 - F_1^* F_4 + \cos\theta\,(F_2^* F_4 - F_1^* F_3)\}\,\rho \tag{A.12}$$

$$\check{O}_{z'} = -\sin^2\theta\,\mathrm{Im}\,\{F_1^* F_3 + F_2^* F_4\}\,\rho \tag{A.13}$$

with $\check{\Sigma} = \Sigma\,\sigma_0$, etc. and $\rho = q/k$.

Appendix B. Expansion of CGLN amplitudes in terms of invariant amplitudes

The CGLN amplitudes are obtained from the invariant amplitudes A_i by the following equations [87]:

$$F_1 = \frac{W - m_N}{8\pi\,W}\sqrt{(E_i + m_N)(E_f + m_N)}\Big(A_1 + (W - m_N)\,A_4 - \frac{2m_N\nu_B}{W - m_N}\,(A_3 - A_4)\Big),$$

$$F_2 = \frac{W + m_N}{8\pi\,W}\,q\sqrt{\frac{E_i - m_N}{E_f + m_N}}\Big(-A_1 + (W + m_N)\,A_4 - \frac{2m_N\nu_B}{W + m_N}\,(A_3 - A_4)\Big),$$

$$F_3 = \frac{W + m_N}{8\pi\,W}\,q\sqrt{(E_i - m_N)(E_f + m_N)}\big((W - m_N)\,A_2 + A_3 - A_4\big),$$

$$F_4 = \frac{W - m_N}{8\pi\,W}\,q^2\sqrt{\frac{E_i + m_N}{E_f + m_N}}\big(-(W + m_N)\,A_2 + A_3 - A_4\big), \tag{B.1}$$

with $\nu_B = (t - m_\eta^2)/(4m_N)$.

Table 7. Background parameters for Born terms and Regge exchanges. The Regge damping parameters Λ_R for η and η' photoproduction are given in units of GeV, the Regge cut parameters d_c in GeV^{-2}, all other parameters are dimensionless. The Regge cut parameters are the same for η and η' photoproduction.

$g^2_{\eta NN}/4\pi$	0.063	$g^2_{\eta' NN}/4\pi$	0.060
$\alpha_{B,\eta}$	4.51	$\alpha_{B,\eta'}$	3.95
$\Lambda_{R,\eta}$	0.974	$\Lambda_{R,\eta'}$	0.440
$\lambda^{\rho}_{\eta\gamma}$	0.910	$\lambda^{\rho}_{\eta'\gamma}$	1.049
$\lambda^{\omega}_{\eta\gamma}$	0.246	$\lambda^{\omega}_{\eta'\gamma}$	0.363
$\lambda^{b_1}_{\eta\gamma}$	0.1	$\lambda^{b_1}_{\eta'\gamma}$	1
g^v_ρ	2.71	g^t_ρ	4.20
g^v_ω	14.2	g^t_ω	0
g_{h_1}/g_{b_1}	0.667	$g^t_{b_1}$	−7.0
$c_{\rho\mathbb{P}}$	4.64	$c_{\omega\mathbb{P}}$	−5.00
$c_{\rho f_2}$	3.10	$c_{\omega f_2}$	1.11
$\tilde{c}_{\rho\mathbb{P}}$	0	$\tilde{c}_{\omega\mathbb{P}}$	0
$\tilde{c}_{\rho f_2}$	0.245	$\tilde{c}_{\omega f_2}$	−0.122
$d_{c,\rho\mathbb{P}}$	12.1	$d_{c,\rho f_2}$	12.1
$d_{c,\omega\mathbb{P}}$	2.09	$d_{c,\omega f_2}$	2.09

Appendix C. Background and Breit-Wigner resonance parameters

In this appendix we list all parameters used in our isobar model. In table 5 we give the hadronic parameters for 21 N^* resonances used in EtaMAID2018. For all of them we found couplings to the ηN channel, and for 12 of them also to the $\eta' N$ channel. Table 6 gives all photon couplings for proton and neutron targets and the newly introduced unitarization phases for all four channels. Finally, table 7 gives all background parameters for Born terms and Regge amplitudes.

References

1. Particle Data Group (M. Tanabashi *et al.*), Phys. Rev. D **98**, 030001 (2018).
2. V. Krusche, C. Wilkin, Prog. Part. Nucl. Phys. **80**, 43 (2015).
3. L. Tiator, Few Body Syst. **59**, 21 (2018).
4. D. Drechsel, O. Hanstein, S.S. Kamalov, L. Tiator, Nucl. Phys. A **645**, 145 (1999) `https://maid.kph.uni-mainz.de/`.
5. D. Drechsel, S.S. Kamalov, L. Tiator, Eur. Phys. J. A **34**, 69 (2007).
6. W.T. Chiang, S.N. Yang, L. Tiator, M. Vanderhaeghen, D. Drechsel, Phys. Rev. C **68**, 045202 (2003).
7. Crystal Ball at MAMI Collaboration (E.F. McNicoll *et al.*), Phys. Rev. C **82**, 035208 (2010) **84**, 029901(E) (2011).
8. CBELSA/TAPS Collaboration (V. Crede *et al.*), Phys. Rev. C **80**, 055202 (2009).
9. CLAS Collaboration (B.A. Mecking *et al.*), Nucl. Instrum. Methods A **503**, 513 (2003).
10. J. Ajaka *et al.*, Phys. Rev. Lett. **81**, 1797 (1998).
11. LEPS Collaboration (M. Sumihama *et al.*), Phys. Rev. C **80**, 052201 (2009).
12. F. Miyahara *et al.*, Prog. Theor. Phys. Suppl. **168**, 90 (2007).
13. Z.p. Li, H.x. Ye, M.h. Lu, Phys. Rev. C **56**, 1099 (1997).
14. B. Saghai, Z.p. Li, Eur. Phys. J. A **11**, 217 (2001).
15. B. Golli, S. Širca, Eur. Phys. J. A **52**, 279 (2016).
16. T. Feuster, U. Mosel, Phys. Rev. C **59**, 460 (1999).
17. R.M. Davidson, N. Mathur, N.C. Mukhopadhyay, Phys. Rev. C **62**, 058201 (2000).
18. B. Borasoy, Eur. Phys. J. A **9**, 95 (2000).
19. D. Ruić, M. Mai, U.G. Meißner, Phys. Lett. B **704**, 659 (2011).
20. I.G. Aznauryan, Phys. Rev. C **68**, 065204 (2003).
21. K. Nikonov, PhD Thesis, Mainz (2018).
22. A. Sibirtsev, J. Haidenbauer, S. Krewald, U.-G. Meißner, Eur. Phys. J. A **46**, 359 (2010).
23. G. Knöchlein, D. Drechsel, L. Tiator, Z. Phys. A **352**, 327 (1995).
24. L. Tiator, D. Drechsel, G. Knöchlein, C. Bennhold, Phys. Rev. C **60**, 035210 (1999).
25. W.T. Chiang, S.N. Yang, L. Tiator, D. Drechsel, Nucl. Phys. A **700**, 429 (2002).
26. V.A. Tryasuchev, Eur. Phys. J. A **22**, 97 (2004).
27. V.A. Tryasuchev, V.A. Serdyutskiy, A.G. Kondratyeva, Phys. At. Nucl. **81**, 62 (2018) Yad. Fiz. **81**, 51 (2018).
28. F. Huang, H. Haberzettl, K. Nakayama, Phys. Rev. C **87**, 054004 (2013).
29. K. Nakayama, Y. Oh, H. Haberzettl, J. Korean Phys. Soc. **59**, 224 (2011).
30. V. Shklyar, H. Lenske, U. Mosel, Phys. Lett. B **650**, 172 (2007).
31. M. Shrestha, D.M. Manley, Phys. Rev. C **86**, 055203 (2012).
32. H. Kamano, S.X. Nakamura, T.-S.H. Lee, T. Sato, Phys. Rev. C **88**, 035209 (2013).
33. D. Rönchen, M. Döring, H. Haberzettl, J. Haidenbauer, U.-G. Meißner, K. Nakayama, Eur. Phys. J. A **51**, 70 (2015).
34. A.V. Anisovich *et al.*, Phys. Rev. C **96**, 055202 (2017).
35. A.V. Anisovich *et al.*, Phys. Lett. B **772**, 247 (2017).
36. D. Rönchen, M. Döring, U.-G. Meißner, Eur. Phys. J. A **54**, 110 (2018).
37. B.C. Hunt, D.M. Manley, arXiv:1804.06031v1 [nucl-ex].
38. I.S. Barker, A. Donnachie, J.K. Storrow, Nucl. Phys. B **95**, 347 (1975).
39. H. Osmanović, M. Hadžimehmedović, R. Omerović, J. Stahov, V. Kashevarov, K. Nikonov, M. Ostrick, L. Tiator, A. Švarc, Phys. Rev. C **97**, 015207 (2018).
40. SAPHIR Collaboration (R. Plötzke *et al.*), Phys. Lett. B **444**, 555 (1998).
41. V. Barger, M. Olsson, Phys. Rev. **151**, 1123 (1966).
42. T. Corthals, J. Ryckebusch, T. Van Cauteren, Phys. Rev. C **73**, 045207 (2006).
43. C. Schmid, Phys. Rev. Lett. **20**, 689 (1968).
44. P.D.B. Collins, R.C. Johnson, G.G. Ross, Phys. Rev. **176**, 1952 (1968).
45. R. Dolen, D. Horn, C. Schmid, Phys. Rev. **166**, 1768 (1968).
46. A. Švarc, M. Hadžimehmedović, H. Osmanović, J. Stahov, L. Tiator, R.L. Workman, Phys. Rev. C **89**, 065208 (2014).

47. A. Švarc, M. Hadžimehmedović, H. Osmanović, J. Stahov, L. Tiator, R.L. Workman, Phys. Rev. C **88**, 035206 (2013).
48. G.F. Chew, M.L. Goldberger, F.E. Low, Y. Nambu, Phys. Rev. **106**, 1345 (1957).
49. J.D. Bjorken, S.D. Drell, *Relativistic Quantum Fields* (McGraw-Hill, New York, 1965).
50. L. Tiator, C. Bennhold, S.S. Kamalov, Nucl. Phys. A **580**, 455 (1994).
51. V.L. Kashevarov, M. Ostrick, L. Tiator, Phys. Rev. C **96**, 035207 (2017).
52. A. Donnachie, Y.S. Kalashnikova, Phys. Rev. C **93**, 025203 (2016).
53. A.V. Anisovich *et al.*, Phys. Lett. B **542**, 8 (2002).
54. A.V. Anisovich *et al.*, Phys. Lett. B **542**, 19 (2002).
55. JPAC Collaboration (J. Nys *et al.*), Phys. Rev. D **95**, 034014 (2017).
56. JPAC Collaboration (V. Mathieu *et al.*), Phys. Rev. D **98**, 014041 (2018).
57. S.M. Flatté, Phys. Lett. B **63**, 224 (1976).
58. A2 Collaboration at MAMI (V.L. Kashevarov *et al.*), Phys. Rev. Lett. **118**, 212001 (2017).
59. CLAS Collaboration (M. Williams *et al.*), Phys. Rev. C **80**, 045213 (2009).
60. A. Bock *et al.*, Phys. Rev. Lett. **81**, 534 (1998).
61. GRAAL Collaboration (O. Bartalini *et al.*), Eur. Phys. J. A **33**, 169 (2007).
62. P. Collins *et al.*, Phys. Lett. B **771**, 213 (2017).
63. A2 Collaboration at MAMI (C.S. Akondi *et al.*), Phys. Rev. Lett. **113**, 102001 (2014).
64. I. Senderovich *et al.*, Phys. Lett. B **755**, 64 (2016).
65. A2 Collaboration at MAMI (L. Witthauer *et al.*), Phys. Rev. Lett. **117**, 132502 (2016).
66. A2 Collaboration at MAMI (L. Witthauer *et al.*), Phys. Rev. C **95**, 055201 (2017).
67. A2 Collaboration at MAMI (D. Werthmüller *et al.*), Phys. Rev. C **90**, 015205 (2014).
68. CBELSA/TAPS Collaboration (I. Jaegle *et al.*), Eur. Phys. J. A **47**, 89 (2011).
69. CBELSA/TAPS Collaboration (L. Witthauer *et al.*), Eur. Phys. J. A **53**, 58 (2017).
70. GRAAL Collaboration (A. Fantini *et al.*), Phys. Rev. C **78**, 015203 (2008).
71. P. Levi Sandri *et al.*, Eur. Phys. J. A **51**, 77 (2015).
72. CBELSA/TAPS Collaboration (I. Jaegle *et al.*), Eur. Phys. J. A **47**, 11 (2011).
73. K.H. Althoff *et al.*, Z. Phys. C **1**, 327 (1979).
74. J. Ahrens *et al.*, Phys. Rev. C **74**, 045204 (2006).
75. Particle Data Group (J. Beringer *et al.*), Phys. Rev. D **86**, 010001 (2012).
76. GRAAL Collaboration (V. Kuznetsov *et al.*), Phys. Lett. B **647**, 23 (2007).
77. V. Kuznetsov *et al.*, Phys. Rev. C **83**, 022201 (2011).
78. A2 Collaboration (D. Werthmüller *et al.*), Phys. Rev. Lett. **111**, 232001 (2013).
79. R.A. Arndt, Y.I. Azimov, M.V. Polyakov, I.I. Strakovsky, R.L. Workman, Phys. Rev. C **69**, 035208 (2004).
80. A.V. Anisovich, E. Klempt, V. Kuznetsov, V.A. Nikonov, M.V. Polyakov, A.V. Sarantsev, U. Thoma, Phys. Lett. B **719**, 89 (2013).
81. D. Diakonov, V. Petrov, M.V. Polyakov, Z. Phys. A **359**, 305 (1997).
82. A.V. Anisovich, V. Burkert, M. Dugger, E. Klempt, V.A. Nikonov, B.G. Ritchie, A.V. Sarantsev, U. Thoma, Phys. Lett. B **785**, 626 (2018).
83. A. Švarc *et al.*, Phys. Rev. C **97**, 054611 (2018).
84. A. Švarc *et al.*, Phys. Rev. C **98**, 045206 (2018).
85. A.M. Sandorfi, B. Dey, A. Sarantsev, L. Tiator, R. Workman, AIP Conf. Proc. **1432**, 219 (2012).
86. R.A. Arndt, W.J. Briscoe, I.I. Strakovsky, R.L. Workman, Phys. Rev. C **66**, 055213 (2002) `http://gwdac.phys.gwu.edu/`.
87. P. Dennery, Phys. Rev. **124**, 2000 (1961).